Published in Geochemistry Geophysics Geosystems (G3) 8, issue 9, 1-25, 2007
which should be used for any reference to this work

Li, Be, and B abundances in minerals of peridotite xenoliths from Marsabit (Kenya): Disequilibrium processes and implications for subduction zone signatures

Benjamin Kaeser

Institut de Géologie et d'Hydrogéologie, Université de Neuchâtel, Rue Emile-Argand 11, CH-2009 Neuchâtel, Switzerland

Now at School of GeoSciences, University of Edinburgh, The King's Buildings, West Mains Road, Edinburgh EH9 3JW, UK (v1bkaser@staffmail.ed.ac.uk)

Angelika Kalt

Institut de Géologie et d'Hydrogéologie, Université de Neuchâtel, Rue Emile-Argand 11, CH-2009 Neuchâtel, Switzerland (angelika.k.alt@unine.ch)

Thomas Ludwig

Mineralogisches Institut, Universität Heidelberg, Im Neuenheimer Feld 236, D-69120 Heidelberg, Germany (tl@min.uni-heidelberg.de)

Keywords: light element geochemistry; secondary ion mass spectrometry; mantle xenoliths; metasomatism.

Index Terms: 1025 Geochemistry: Composition of the mantle; 1033 Geochemistry: Intra-plate processes (3615, 8415); 1065 Geochemistry: Major and trace element geochemistry; 3625 Mineralogy and Petrology: Petrography, microstructures, and textures.

[1] The light elements Li, Be, and B have been analyzed in situ in minerals from three groups of peridotite xenoliths hosted in Quaternary basanites from the Marsabit volcanic field (northern Kenya). Group I and II are fertile lherzolites that experienced deformation, decompression, and cooling in the context of Mesozoic rifting (Group I), followed by heating, static recrystallization, and associated cryptic metasomatism (Group II) as a result of Tertiary-Quaternary rifting and magmatism. Group III xenoliths are spinel harzburgites and dunites that experienced strong cryptic and modal metasomatism. The Li-Be-B systematics in minerals of Group I and II are similar to unmetasomatized subcontinental lithospheric mantle. In contrast, Group III samples are characterized by significant enrichment in all light elements and disequilibrium partitioning between different phases. Light element concentrations levels are similar to that expected for mantle rocks metasomatized by melts and fluids released from subducting slabs, while light element/rare earth element ratios (especially Li/Yb) approach those of typical Island Arc basalts. However, detailed investigation of textures and chemical zoning shows that at least Li concentrations in primary minerals were modified (i.e., decoupled from Yb) during late-stage melting and/or fluid percolation related to Tertiary-Quaternary alkaline magmatism in Marsabit (formation of melt pockets consisting of silicate glass, clinopyroxene, olivine, and chromite), ultimately followed by xenolith entrapment and transport to the surface. Mass balance calculations show that the melt pockets formed at the expense of earlier metasomatic phases. During this process the melt pockets mostly preserved the B, Be, and rare earth element budget of the precursor phase assemblage, whereas Li was added. Elevated B/Be and low Ce/B of metasomatic phases prior to late melting could result from metasomatism by a slab fluid. However, similar characteristics are expected for evolved Si- and CO_2-rich fluids derived from basanite melt-peridotite interaction, not related to any subduction zone process. The results of this study imply that the inference of a "slab signature" exclusively based on trace element data of metasomatized peridotite is ambiguous.

1. Introduction

[2] The geochemistry of the low atomic mass elements Li, Be and B (hereafter called ''light elements'') is increasingly used to constrain metasomatic and magmatic processes in the Earth's mantle and in volcanic rocks. Li, Be and B systematics (including Li and B isotopes) are modified in the oceanic lithosphere during interaction with seawater making the light elements useful to detect and track subducted components either in volcanic products [e.g., *Ryan and Langmuir*, 1987, 1988, 1993; *Ishikawa and Nakamura*, 1994; *Brenan et al.*, 1998a, 1998b; *Chan and Kastner*, 2000; *Leeman and Sisson*, 2002; *Tomascak et al.*, 2002; *Elliott*, 2003; *Elliott et al.*, 2004], metamorphic rocks [*Bebout et al.*, 1993; *Peacock and Hervig*, 1999; *Zack et al.*, 2003; *Marschall et al.*, 2006] or mantle rocks [*Scambelluri et al.*, 2004, 2006; *Paquin et al.*, 2004] from convergent tectonic settings.

[3] The question to which extent light elements can be used as tracers for long-time crust-mantle recycling is currently highly debated. Recent studies, for example, report Li isotope ratios in mantle rocks from continental rifts [e.g., *Brooker et al.*, 2004; *Nishio et al.*, 2004] and in mid-ocean ridge basalts (MORB) [*Elliott et al.*, 2006] that can be explained in terms of components that reflect fluid-mediated processes in subduction zones (i.e., dehydration of subducting lithosphere causing Li isotope depletion in the recycled slab and enrichment in the overlying peridotitic mantle wedge [e.g., *Tomascak et al.*, 2002]). On the other hand, there is evidence from mantle xenoliths that intraplate mantle metasomatism can lead to significant light element enrichment (e.g., Li enrichment in olivine by carbonatite and/or silicate melt [*Seitz and Woodland*, 2000; *Woodland et al.*, 2004] or B enrichment in clinopyroxene by fluids [*Ottolini et al.*, 2004]). Further, *Seitz et al.* [2004] suggested that Li isotope fractionation, e.g., between olivine and clinopyroxene, occurs also at high temperatures in the mantle. This is supported by recent experiments that provide evidence for both temperature-dependent fluid/mineral isotope fractionation (in the order of 1‰ at 900°C between clinopyroxene and aqueous fluid [*Wunder et al.*, 2006]) and kinetic fractionation as a result of different diffusivities of ^{6}Li and ^{7}Li in melts [*Richter et al.*, 2003; *Lundstrom et al.*, 2005] and minerals (e.g., diopside [*Coogan et al.*, 2005]). Detailed in situ measurements of Li isotopes in minerals from mantle xenoliths and mafic lavas show that diffusion during late-stage mantle metasomatism [*Jeffcoate et al.*, 2007; *Rudnick and Ionov*, 2007] or melt-mineral reaction in lavas [*Parkinson et al.*, 2007] can produce strong grain-scale Li heterogeneity, with respect to both concentrations and isotope compositions. The results of such processes open the possibility that the ''slab signature,'' at least in terms of Li systematics, is not distinctive.

[4] In summary, the potential of light elements as tracers for different mantle processes is far from being fully understood. This comes also from the fact that most previous light element studies mainly focused on Li systematics while data sets including B and Be are still scarce, and the influence of intraplate mantle metasomatism on light elements compared to classical trace elements, such as the rare earth elements (REE), remains poorly investigated [*Ottolini et al.*, 2004; *Raffone et al.*, 2006].

[5] In this study we report Li, Be and B abundances in minerals from peridotite xenoliths (Marsabit, Kenya). Earlier petrological and geochemical studies have shown that the uppermost mantle in this region is compositionally and structurally strongly heterogeneous as a result of rifting-related thinning and uplift in the Mesozoic and reheating accompanied by cryptic and modal metasomatism

related to the development of the East African Rift System (EARS) and the Tertiary-Quaternary Marsabit magmatic system [*Henjes-Kunst and Altherr*, 1992; *Kaeser et al.*, 2006, 2007]. It is therefore a very suitable case to investigate the systematics of the light elements in mantle rocks that experienced various processes, including different styles of subsolidus mineral reactions, mantle metasomatism resulting from fluid and/or melt infiltration and late-stage melting phenomenon. The aim of the study is to put new constraints on the light element content of subcontinental mantle, as well as to investigate to which extent light element abundances can be used as tracers for subducted material in intraplate tectonic settings.

2. Sample Context and Results From Earlier Studies

[6] The Marsabit mantle xenoliths are hosted by Quaternary basanitic and alkali-basaltic scoriae from cinder cones on the Marsabit shield volcano (northern Kenya, about 150 km eastward of Lake Turkana [see *Henjes-Kunst and Altherr*, 1992]). Besides minor pyroxenite, the major rock types are different groups of mantle peridotite on which this study focuses. They are distinguished on the basis of textures and mineralogical composition (for details, see *Kaeser et al.* [2006]) and include porphyroclastic formerly garnet-bearing spinel lherzolites, hereafter referred to as (grt)-spl lherzolites (Group I; Figure 1a), granular statically recrystallized (grt)-spl lherzolite (Group II; Figure 1b) and cryptically and modally metasomatized spl harzburgite and dunite (Group III; Figure 1c). Group III is further subdivided into three subtypes (Type III-a to -c; see below). The Marsabit mantle xenoliths were earlier investigated in detail for textures, mineralogy, major and trace element geochemistry and thermobarometry [*Henjes-Kunst and Altherr*, 1992; *Kaeser et al.*, 2006]. Metasomatism and melting features in Group III xenoliths are further addressed in a separate paper [*Kaeser et al.*, 2007]. The results of these earlier studies are summarized in the following (note that primary olivine (ol), clinopyroxene (cpx) and orthopyroxene (opx), even when cryptically metasomatized, will be referred to as ol-I, cpx-I, and opx-I, whereas newly crystallized ol, cpx, chromite (micro-phenocrysts in melt pockets) and metasomatic opx (contains phlogopite inclusions) will be named Ol_m, Cpx_m, Chr_m and Opx_m, respectively (where m stands for ''metasomatic'')).

2.1. Rift-Related Thinning of the Continental Lithosphere

[7] The possibly oldest features of the lithospheric mantle beneath Marsabit are preserved in Group I (grt)-spl lherzolites. These rocks provide evidence of an earlier high-pressure/high-temperature stage ($\sim$970–1100°C at depths around 60–90 km; mainly based on geothermobarometers of *Brey and Köhler* [1990]; see *Kaeser et al.* [2006] for details), similar to nonrifted subcontinental lithospheric mantle, such as actually present underneath southern Kenya [*Henjes-Kunst and Altherr*, 1992]. This stage most likely corresponds to the lithospheric conditions prior to continental rifting. All three peridotite types show indications for later cooling, decompression and pervasive deformation (to very low mantle *P-T* conditions of $\sim$700–800°C at depths $\sim$30–40 km), which is interpreted to reflect the results of rift-related lithospheric thinning. During these events Group I and II rocks passed from the garnet- into the spinel-stability field, which is indicated by the presence of spl-opx-cpx symplectites (ubiquitous in Group I and II, rare in Group III) and by the preservation of ''garnet signatures'' in Group I samples (low HREE and Al concentrations in cpx-I cores [*Kaeser et al.*, 2006]). The cpx-rich nature of Group I xenoliths is interpreted to reflect subsolidus mixing between former grt websterite and peridotite during deformation, supported by the presence of centimeter-sized cpx- and symplectite-rich layers [*Kaeser et al.*, 2006, Figure 2a]. Small amounts of Ti-pargasite and phlogopite (Table 1) in Group I samples are most likely derived from this pyroxenitic component. Although volcanism in Marsabit is related to the young EARS, the volcano itself is situated within the older Anza rift [e.g., *Morley et al.*, 2006], about 150 km eastward of the EARS. Therefore rifting-related features preserved in the underlying mantle were interpreted to be more likely of Mesozoic-Paleogene (Anza-related) rather than of Tertiary-Quaternary age (EARS-related; see *Kaeser et al.* [2006] for details).

2.2. Reheating, Recrystallization, Metasomatism

[8] Group II and III xenoliths provide evidence for a later thermal event associated with metasomatism. During this event older features (rifting-related; see above) were obliterated, indicating that metasomatizing agents are most likely related to the development of the EARS and the Marsabit magmatic system. In Group II xenoliths, reheating (up to $\sim$1100°C at <1.5 GPa [*Kaeser et al.*, 2006])

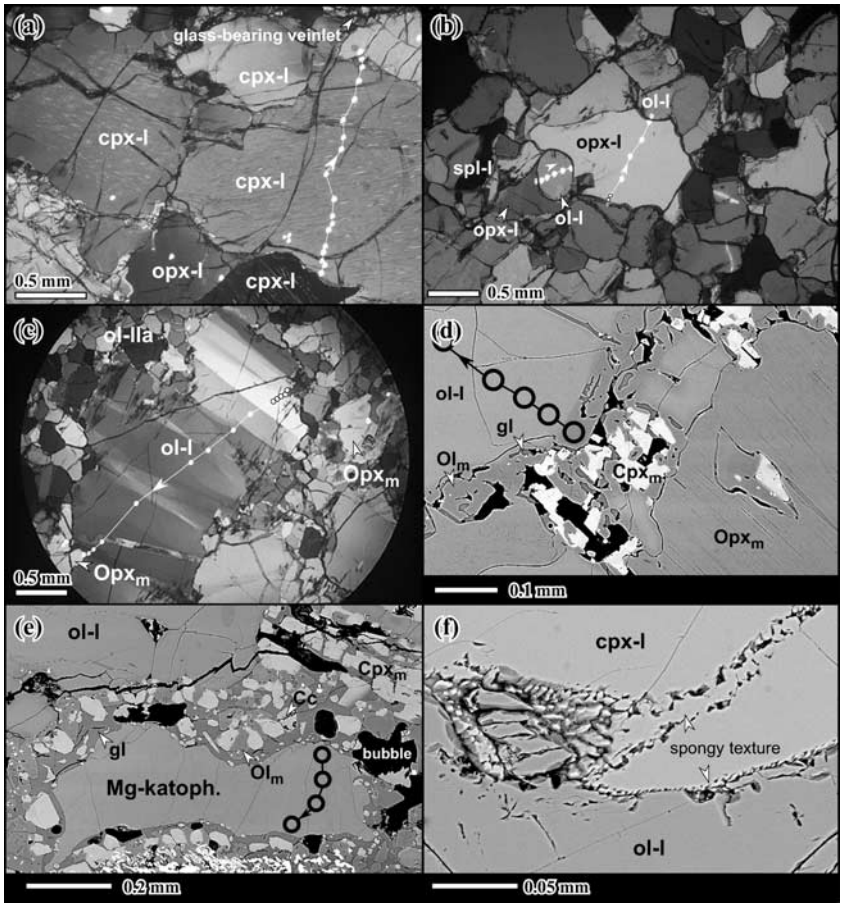

Figure 1. Photomicrographs (Figures 1a–1c; crossed polarizers) and back-scattered electron images (Figures 1d–1f) showing textural aspects of the investigated peridotite xenoliths from Marsabit. (a) Cpx-I (with opx exsolution lamellea) and opx-I in Group I, xenolith Ke 1963/2 (porphyroclastic (grt)-spl lherzolite). White dots are SIMS spots of the profile depicted in Figure 3a (arrow indicates from right to left). (b) Strain-free, granular fabric in Group II, xenolith Ke 1958/20 (recrystallized (grt)-spl lherzolite). White dots are SIMS spots of profiles across opx-I (Figure 3c) and ol-I (Figure 3d). (c) Fabric of Group III-c, xenolith Ke 1965/3 (porphyroclastic spl dunite). Note strongly kinked olivine porphyroclast (ol-I) and strain-free, polygonal neoblasts (ol-IIa). White dots are SIMS spots of the profile depicted in Figure 5b. (d) Glass + microlites at contact between ol-I and Opx_m in Group III-c, xenolith Ke 785* (porphyroclastic spl harzburgite). Black circles indicate the SIMS profile depicted in Figure 5a. (e) Residual Mg-katophorite in a melt pocket (glass + microlites) in Group III-c, xenolith Ke 785*. Black circles indicate SIMS profile depicted in Figure 5c. (f) Late-stage ''spongy'' clinopyroxene rims developing at a glass-free contact between cpx-I and ol-I in Group II, xenolith Ke 1958/13 (recrystallized (grt)-spl lherzolite).

was accompanied by static recrystallization and cryptic metasomatism (i.e., enrichment of cpx-I in FeO, TiO_2, LREEs, U, Th and Nb relative to Group I clinopyroxene). Calculated trace element patterns of melts in equilibrium with Group II xenoliths indicates that metasomatizing agents were silicate mafic melts compositionally similar (and possibly genetically related) to the Quaternary basanites erupted at the surface of Marsabit [*Kaeser et al.*, 2006].

[9] Further evidence for Tertiary-Quaternary metasomatism can be found in the porphyroclastic Group III peridotite xenoliths (Group III), which show a textural transition from cryptically metasomatized spl harzburgite (Type III-a) via cpx-I-bearing (III-b) to cpx-I-free (III-c) modally metasomatized harzburgite and dunite. The latter two contain metasomatic orthopyroxene (Opx_m), amphibole (Mg-katophorite), Na-rich phlogopite, graphite and apatite. The phase assemblage, *P-T* conditions (<1.5 GPa), as well as major and trace element characteristics indicate that this type of metasomatism resulted from the infiltration of volatile (H_2O, CO_2)-rich Si-rich fluid and/or melt in a preexisting heterogeneous mantle [*Kaeser et al.*,

Table 1. Details of the Investigated Peridotite Xenoliths[a]

			Primary Minerals, vol%					Modal Metasomatism, vol%		P-T Estimates		
										Final Stage[d]		m.p.[e]
Sample	Group	Lithology	Former Garnet[b]	ol-I	opx-I	cpx-I	spl-I	Early Metasomatic Phases[c]	Melt Pockets (m.p.)	P, GPa	T, °C	T, °C
1963/2	I	porphyroclastic (grt)-spl lherzolite	15.5	41.1	23.2	19.2	0.1	Ti-pargasite (0.8), phlogopite (0.1)	–	<1.47	799 ± 25	–
1958/13	II	recrystallized (grt)-spl lherzolite	9.9	58.0	20.2	10.3	0.2	–	–	<1.66	908 ± 40	–
1958/20	II	recrystallized (grt)-spl lherzolite	14.8	52.0	23.7	9.3	0.3	–	–	<1.63	1068 ± 20	–
1965/1	III-a	porphyroclasticspl harzburgite	1.5	70.8	22.9	3.9	0.9	graphite (tr.)	–	<1.62	834 ± 37	–
1965/15	III-b	porphyroclasticspl harzburgite	–	71.9	17.7	6.8	0.4	Mg-katophorite (0.15), phlogopite (0.1),[f] graphite (0.1), apatite (tr.)	3 vol% (cpx_m, ol_m, chr_m, Mg-calcite, silicate glass)	–	837 ± 46	–
1965/3	III-c	porphyroclasticspl dunite	–	80.1	–	–	0.7	low-Al Opx_m (3.2); phlogopite (tr.; inclusions in Opx_m)	16 vol% (cpx_m, ol_m, chr_m, Mg-calcite, silicate glass)	–	719 ± 6	1246 ± 136
785*	III-c	porphyroclasticspl harzburgite	–	64.0	–	–	0.6	low-Al Opx_m (18.7), Mg-katophorite (1.1), phlogopite (0.6), graphite (tr.)	14.4 vol% (cpx_m, ol_m, chr_m, Mg-calcite, silicate glass)	<1.89	751 ± 10	1234 ± 85

[a] Notes: ol-I, opx-I, cpx-I and opx-I: primary (i.e., not metasomatic) olivine, orthopyroxene, clinopyroxene, and spinel, respectively (porphyroclasts and neoblasts undifferentiated); Cpx_m, Ol_m, Chr_m: Na-rich Cr-diopside, olivine, and chromite micro-phenocrysts in melt pockets, respectively.

[b] Spl-opx-cpx symplectites.

[c] Formed prior to glass-bearing melt pockets (see text for details; numbers in brackets are vol%; tr., traces).

[d] After cooling and decompression (max. *P* obtained using the Cr content in spl-I [*Carroll Webb and Wood*, 1986]; *T* based on the Ca-in-opx thermometer of *Brey and Köhler* [1990] and calculated for an assumed *P* of 1.2 GPa).

[e] *T* obtained from the Fe-Mg partitioning between Ol_m and Chr_m (thermometer of *Ballhaus et al.* [1991]; calculated at assumed *P* of 1.2 GPa).

[f] No phlogopite was found in the thin section used for SIMS analysis; n.d., not detected; dash (–), not calculated.

2007]. Si-saturation is indicated by the presence of Opx_m and, at these low pressures, excludes metasomatism by a carbonatitic melt [e.g., *Lee and Wyllie*, 2000]. The occurrence of Group II samples with cpx-I trace element patterns intermediate between typical Group II and Group III cpx indicates that metasomatism in both groups is the result of one single event, but reflecting different compositions of metasomatizing agents as a result of melt-rock reaction and different physical conditions (P-T, fO_2 [see *Kaeser et al.*, 2007]).

2.3. Late-Stage Melting

[10] The latest event consists of partial melting of earlier phases in all peridotite types (mainly amphiboles, but also opx-I, Opx_m, cpx-I, phlogopite, and apatite; see Figures 1d and 1e). Melting occurred most likely shortly before or during the xenolith transport in the host magma (see section 5.1). The result are "melt pockets" [e.g., *Ionov et al.*, 1994] consisting of newly formed minerals (micro-phenocrysts of Cpx_m, Chr_m and Ol_m), silicate glass (quenched melt) and carbonate globules (Mg-calcite). In some cases (especially in Group II samples) cpx-I and spl-I developed typical "spongy" rims [e.g., *Ionov et al.*, 1994; *Shaw et al.*, 2006] (see Figure 1f) composed of empty vugs and secondary Cpx_m or Chr_m respectively. The composition of silicate glass and mass balance calculations clearly show that melt pockets did not result from interaction between the xenoliths and their host magma, but formed by incongruent melting of amphibole ± orthopyroxene ± phlogopite (see *Kaeser et al.* [2007] and section 6.3). Ubiquitous empty bubbles in glass and occasionally high amounts of Mg-calcite suggest that melting was triggered by infiltration of a CO_2-bearing fluid.

3. Li, Be, and B Abundances in Minerals

[11] Abundances of the light elements Li, Be and B were measured in all silicates and in melt pocket glass of 7 xenoliths including at least one representative sample of each peridotite group (Table 1). We analyzed mineral pairs (rim-rim contacts), as well as traverses across single grains to obtain information on zoning (for analytical methods, see Appendix A). Representative concentrations and relative analytical uncertainties (2σ), along with major element data, are given in Table 2. The complete data set is available as auxiliary material[1] (Table S1). The ranges and average abundances of Li, Be and B for each mineral are illustrated in Figure 2. Generally, minerals in both porphyroclastic and statically recrystallized formerly grt-bearing lherzolites (Groups I and II) carry less light elements than the metasomatic spl harzburgites (Type III-a to -c). The latter are further characterized by a larger variation of light element abundances which is mainly due to significant zoning of minerals (Figures 3–5). In the modally metasomatized harzburgites (Type III-b and -c), both the primary anhydrous silicates and the newly formed volatile-bearing minerals (amphibole and phlogopite) are variably enriched in Li, Be, and B compared to Group I and II samples. Silicate glass is the phases with the highest light element concentrations, but shows strong variation from one sample to another (Table 2 and Figure 2).

3.1. Lithium

[12] Among the primary anhydrous minerals (ol-I, opx-I, cpx-I) in the studied mantle xenoliths, olivine is the major carrier of Li. In the formerly grt-bearing rocks (Groups I and II), Li abundances decrease from olivine (1.27–1.86 μg/g) via clinopyroxene (0.59–1.10 μg/g) to orthopyroxene (0.56–1.02 μg/g). Group I Ti-pargasite and phlogopite have the lowest Li concentrations (0.48–0.69 and 0.73–0.86 μg/g, respectively).

[13] Compared to Groups I and II, all minerals from the metasomatized spl harzburgites (Type III-a to -c) are enriched in Li and show considerable compositional variation (Figure 2), as a result of both zoning (Figures 4 and 5) and intergrain heterogeneity (e.g., opx-I core compositions in sample Ke 1965/1 change from ~1.0 to ~2.2 μg/g over a few centimeters). Average abundances (Figure 2) are in the order of 2.5–5.3 μg/g (ol-I), 1.6–2.0 μg/g (cpx-I), and 1.4–3.2 μg/g (opx-I and Opx_m). Mg-katophorite and Na-rich phlogopite contain 2.48–5.17 μg/g and 0.63–5.14 μg/g Li. High concentrations are found in Ol_m and Cpx_m microlites in melt pockets (up to 9.54 μg/g and 5.71 μg/g, respectively). The associated glass shows the highest Li abundances (9.72–22.0 μg/g; Figure 2). These concentrations are higher than those reported from glass of mineralogically similar melt pockets found in xenoliths from Victoria, Australia (3.17–10.9 μg/g [*Woodland et al.*, 2004]).

[1]Auxiliary materials are available at ftp://ftp.agu.org/apend/gc/2006gc001555.

Table 2. (Representative Sample). Representative Major and Light Element Compositions of Minerals in the Investigated Peridotite Xenoliths From Marsabit[a] [The full Table 2 is available in the HTML version of this article at http://www.g-cubed.org]

	Ke 1963/2: Group I (grt)-spl Lherzolite								Ke 1958/13: Group II Recrystallized (grt)-spl Lherzolite				
Sample													
Mineral	ol-I	ol-I	cpx-I	cpx-I	opx-I	opx-I	Ti-prg	Phl	ol-I	ol-I	cpx-I	cpx-I	opx-I
Location	core	core	rim (cpx-I)	core	rim (cpx-I)	core	core	core	rim (cpx-I)	core	rim (opx-I)	core	rim (ol-I)
SiO_2	41.11	40.30	53.13	53.05	56.60	56.38	43.24	38.97	40.75	40.69	53.00	52.33	55.81
TiO_2	n.d.	n.d.	0.66	0.71	0.05	0.18	2.96	4.62	0.00	0.01	0.33	0.43	0.06
Al_2O_3	0.03	0.01	5.34	5.30	2.19	2.48	14.68	15.00	0.01	0.03	5.69	6.47	3.45
Cr_2O_3	n.d.	0.01	0.84	0.78	0.19	0.31	0.37	0.84	0.04	0.03	0.69	0.99	0.24
FeO (tot)	10.25	10.53	2.54	2.74	6.79	6.64	3.73	3.96	9.82	9.34	2.51	2.44	6.14
MnO	0.15	0.21	0.07	0.09	0.18	0.15	0.06	0.03	0.19	0.14	0.08	0.10	0.19
NiO	0.37	0.34	0.08	n.d.	0.08	0.02	0.11	0.21	0.36	0.40	n.a.	n.a.	n.a.
MgO	48.95	48.61	14.95	15.15	34.48	34.02	17.50	21.74	49.26	49.10	15.81	14.61	33.64
CaO	0.02	0.02	20.98	20.04	0.31	0.42	11.54	0.09	0.05	0.06	20.19	20.38	0.65
Na_2O	n.d.	n.d.	1.91	2.20	0.04	0.04	3.67	0.81	0.01	0.02	1.79	2.08	0.11
K_2O	n.d.	n.d.	n.d.	n.d.	n.d.	n.d.	0.41	9.28	n.d.	n.d.	n.d.	n.d.	n.d.
Total	**100.88**	**100.01**	**100.50**	**100.06**	**100.91**	**100.64**	**98.27**	**95.55**	**100.49**	**99.81**	**100.10**	**99.84**	**100.28**
Mg number	89.49	89.17	91.30	90.80	90.05	90.13	89.33	90.73	89.94	90.36	91.82	91.45	90.72
Li	1.337 (37)	1.270 (31)	0.675 (34)	0.804 (21)	0.617 (31)	0.635 (34)	0.695 (30)	0.857 (32)	1.441 (29)	1.536 (33)	0.779 (26)	0.905 (28)	0.684 (22)
Be	n.d.	n.d.	0.093 (6)	0.094 (7)	0.008 (3)	0.010 (2)	0.195 (14)	0.126 (6)	*0.002 (1)*	*0.001 (1)*	0.130 (9)	0.157 (15)	0.035 (3)
B	0.059 (15)	0.041 (9)	0.067 (19)	0.067 (9)	0.044 (13)	0.063 (7)	0.137 (28)	0.708 (31)	0.086 (21)	0.086 (11)	0.100 (16)	0.089 (16)	0.055 (8)

[a] Major element compositions are in wt%; light element compositions are in μg/g. Minerals adjacent to rim analyses are indicated in brackets. Mg numbers: atomic $Mg/(Mg + Fe_{tot}) \times 100$. Numbers in brackets are analytical uncertainties (expressed as 2σ). Values in italic are below the minimal detectable value (L_D of *Currie* [1968]; see Appendix A for definition). Abbreviations: n.d., not detected (i.e., <0.1 wt% for major elements and zero counts during SIMS analysis for Li, Be and B); n.a.: not analyzed; katoph., Mg-katophorite. Opx_m is metasomatic, low-Al orthopyroxene containing phlogopite inclusions. Ol_m and Cpx_m are melt pocket olivine and diopside microlites, respectively.

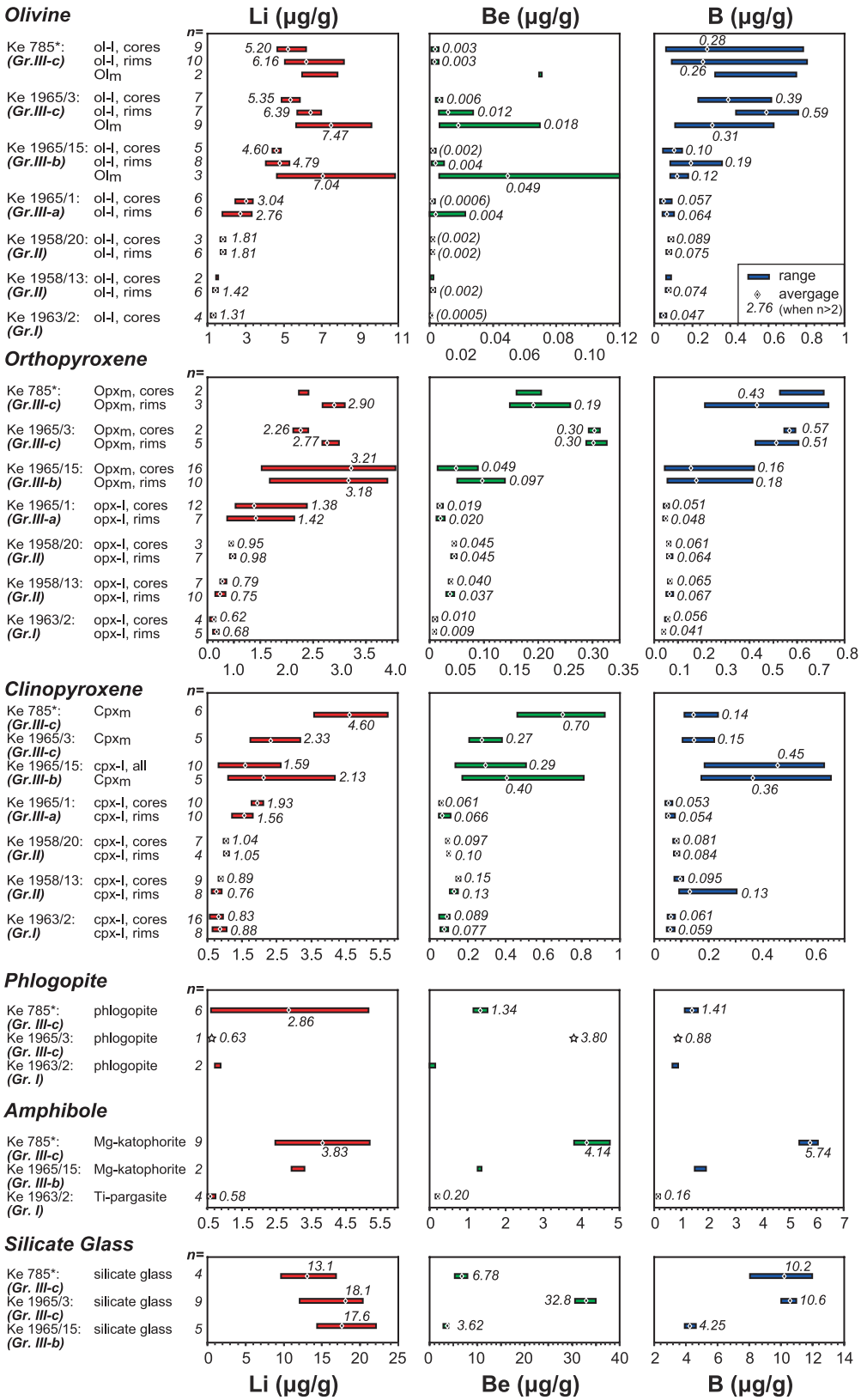

Figure 2. Averages and ranges of Li, Be, and B concentrations in minerals and silicate glass of peridotite xenoliths from Marsabit. Numbers in brackets (essentially Be in olivine) are concentrations below the minimal detectable value L_D [*Currie*, 1968] and are therefore only qualitative values (i.e., above L_C of *Currie* [1968]).

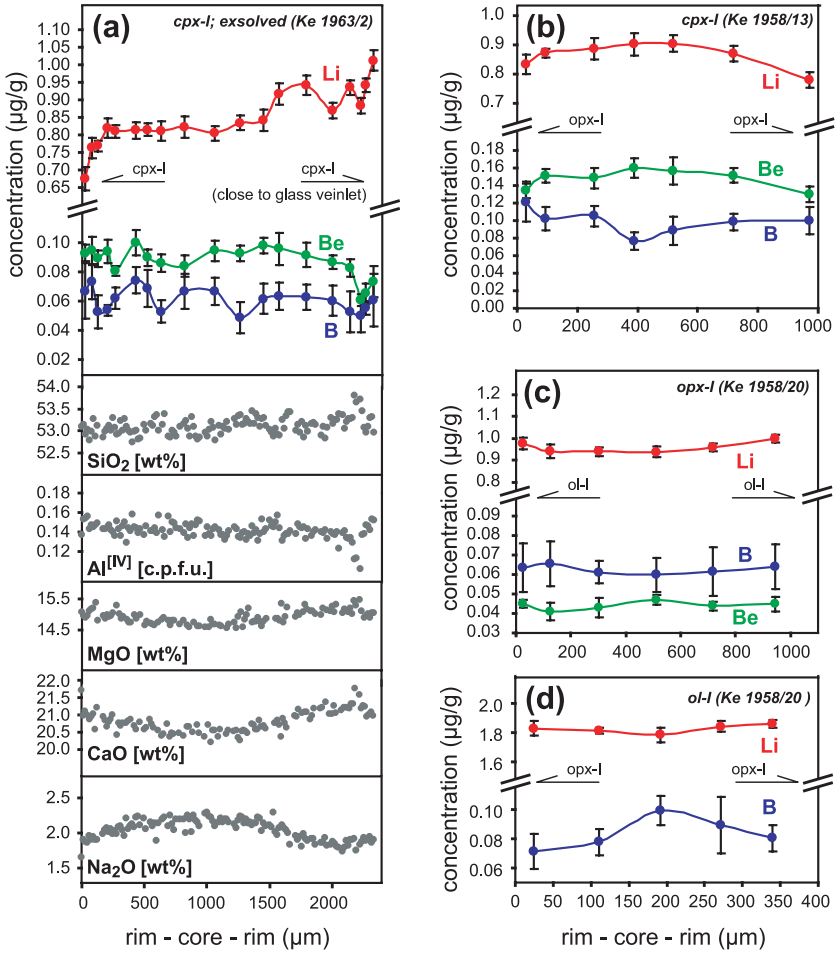

Figure 3. Li, Be, and B (SIMS) and major element (electron microprobe) profiles across minerals from Group I and Group II peridotite xenoliths from Marsabit. (a) Li-Be-B and major element zoning in a clinopyroxene porphyroclast (cpx-I) from Group I sample Ke 1963/2. (b) Li-Be-B zoning in a cpx-I grain from Group II sample Ke 1958/13. Li-Be-B zoning in (c) an opx-I and (d) an ol-I grain of the completely equilibrated Group II sample Ke 1958/20. Arrows pointing to the left and to the right indicate the respective neighboring phase. Error bars correspond to 2σ of single analyses.

3.2. Beryllium

[14] Besides glass, amphibole and phlogopite are the major hosts for Be (up to 4.72 μg/g in Type III-c Mg-katophorite, and 3.80 μg/g in Type III-c phlogopite). However, large variations were observed between different samples (e.g., very low Be abundances in Ti-pargasite and phlogopite from the Group I xenolith; Figure 2). In anhydrous silicates of Groups I, II, and Type III-a, Be exhibits only limited variation (Figure 2). Concentrations decrease from cpx-I (0.055–0.16 μg/g), via opx-I (0.007–0.049 μg/g), to olivine (at the ng/g level, mostly close or below the limit of detection; Table 2). Clinopyroxene and orthopyroxene in the modally metasomatized spl harzburgites (Type III-b to -c), on the other hand, show considerable Be enrichment (0.14–0.50 μg/g in cpx-I, and 0.016–0.32 μg/g in opx-I and Opx_m; Figure 2). Clinopyroxene in melt pockets shows the highest Be concentrations (0.17–0.91 μg/g), and even olivine microlites (Ol_m) contain detectable amounts of Be (up to 0.12 μg/g). By far the highest Be concentrations were measured in silicate glass (up to 34.9 μg/g; Table 2).

3.3. Boron

[15] B in anhydrous silicates from Group I and II lherzolites shows only limited variation and is evenly distributed between ol-I (0.038–0.099 μg/g), cpx-I (0.049–0.092 μg/g; one analysis with 0.30 μg/g), and opx-I (0.039–0.074 μg/g). Minerals in the Type III-a spl harzburgite show the same range of B

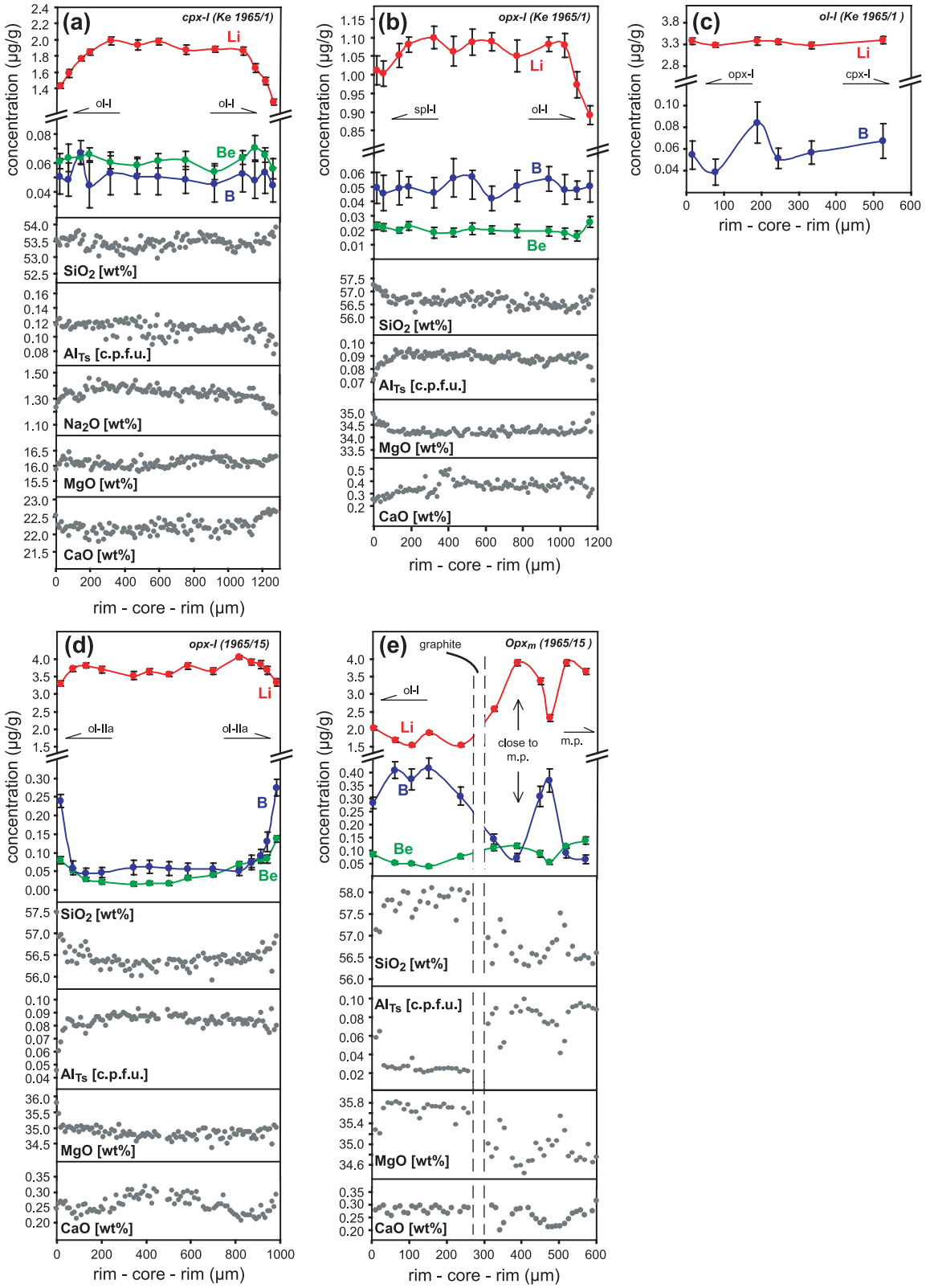

Figure 4. Li, Be, and B (SIMS) and major element (electron microprobe) profiles across minerals from Type III-a and -b spl harzburgite xenoliths. (a) Cpx-I and (b) opx-I porphyroclasts in the Type III-a xenolith Ke 1965/1. (c) Ol-I and (d) opx-I porphyroclasts and (e) metasomatic orthopyroxene (Opx_m) in the amphibole-bearing Type III-b xenolith Ke 1965/15. Error bars correspond to 2σ; m.p. refers to "melt pockets."

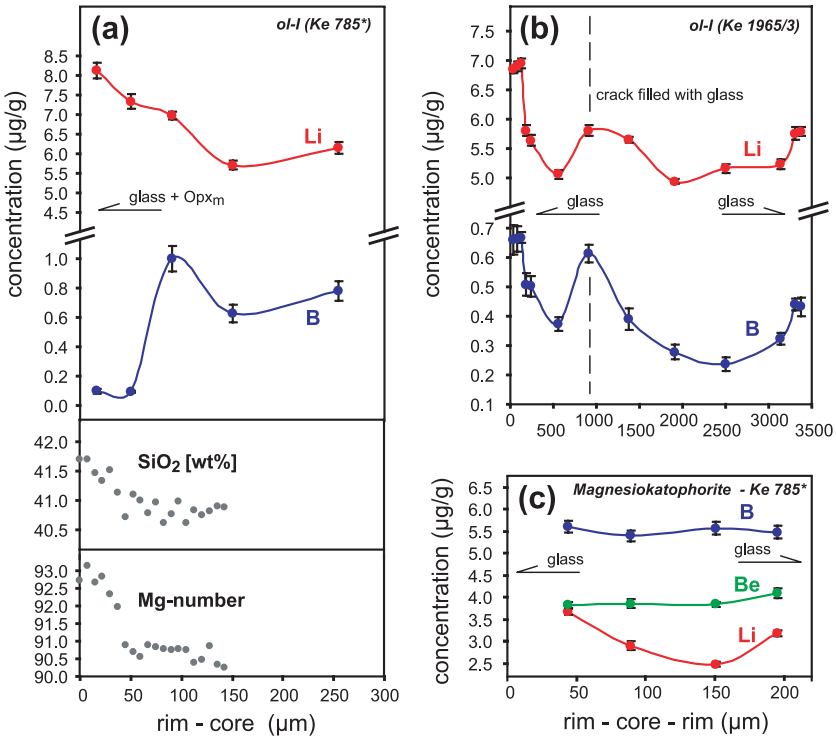

Figure 5. Li, Be, and B (SIMS) and major element (electron microprobe) profiles across minerals from Type III-c spl harzburgite (Ke 785*) and dunite (Ke 1965/3) xenoliths. Olivine porphyroclasts (ol-I) adjacent to silicate glass in samples (a) Ke 785* and (b) Ke 1965/3. (c) Relic Mg-katophorite in melt pocket in sample Ke 785*. Error bars correspond to 2σ.

abundances, while ol-I (0.050–0.80 μg/g) and Opx$_m$ (up to 0.73 μg/g) in Type III-b and -c xenoliths are B-enriched. The high B contents in cpx-I from sample Ke 1965/15 result most likely from tiny amphibole lamellae, inevitably included in some analyses (Table 2). Ti-pargasite (0.13–0.20 μg/g) and phlogopite (0.71–0.87 μg/g) in sample Ke 1963/2 (Group I) show slightly elevated concentrations, but nonetheless, compared to Mg-katophorite and Na-rich phlogopite from Type III-b and -c xenoliths, they are B-depleted (Figure 2). Mg-katophorite in sample Ke 785* contains up to 6.02 μg/g B. Within the melt pocket assemblage, silicate glass is the major host for B (4.01–11.9 μg/g), followed by Ol$_m$ (0.088–0.75 μg/g), and Cpx$_m$ (0.11–0.65).

3.4. Light Element Zoning

[16] Mineral zoning profiles for light elements and major elements (where available) are illustrated in Figures 3–5. Considering the relative analytical uncertainties (2σ), zoning was in most cases restricted to Li and is generally more developed in the cryptically and modally metasomatized spl harzburgites (Type III-a to -c). Further, core-rim zoning strongly depends on the phase adjacent to the analyzed grain. All minerals in contact with silicate glass (irrespective of xenolith group) display Li enrichment on the outermost ~150 μm (Figure 4e or Figures 5a and 5b). Further, Li enrichment of olivine adjacent to glass can be accompanied either by increasing or decreasing B contents (Figure 5). The latter is confined to zones were olivine is in contact with resorbed Opx$_m$ or Cpx$_m$-poor melt pockets (such as displayed in Figure 1d).

[17] A second type of zoning pattern occurs in pyroxenes (but not in olivine) in sample zones devoid of glass. There (irrespective of the neighboring phases) Li abundances decrease on the outermost 150–200 μm (Figures 3a and 3b and 4a–4d). The different behavior of Li, depending on the presence of glass, can be observed on a very small scale. For example, the analyzed cpx-I from the Group I xenolith (Ke 1963/2; Figure 3a) shows decreasing Li abundances at the contact with another cpx-I grain, whereas the other side of the grain (at ~2.5 mm distance), in the vicinity of a tiny glass veinlet (Figure 1a), is significantly enriched in Li. Significant Be and B zoning was

only observed in orthopyroxene from sample Ke 1965/15 (Type III-b; Figure 4d) showing increasing abundances toward opx-I rims.

[18] Profiles where major element data are available show that that light element zoning is sometimes coupled with major element variation. Mg#s in olivine adjacent to glass, for example, always increase simultaneously with Li abundances (e.g., Figure 5a). In pyroxenes from Group III harzburgites, decreasing Li abundances coincide with decreasing $^{[IV]}$Al, CaO and Na_2O, while SiO_2 and MgO contents slightly increase. In a composite low-Al Opx_m grain Li and Be patterns are parallel to the $^{[IV]}$Al profile, whereas B mimics the SiO_2 and MgO patterns (Figure 5e).

4. Partitioning of Li, Be, and B: Degree of (Dis)equilibrium

[19] As the xenoliths from Marsabit display complex metasomatic features, it is important to constrain to what extent chemical equilibrium was attained in the different phase assemblages during their evolution. In the following we will show that minerals from Group I and II xenoliths exhibit near-equilibrium partitioning of light elements. In the case of the Group III spl harzburgites and dunites minerals are generally out of equilibrium. The exception are Cpx_m and Ol_m microlites and silicate glass in melt pockets that occasionally attained equilibrium with respect to Li concentrations.

4.1. Groups I and II

[20] Minerals from Group I and II lherzolites are all characterized by limited variations in light elements and concentration levels overlapping with those defined for ''normal'' mantle peridotite (Figures 2 and 6) [*Seitz and Woodland*, 2000; *Ottolini et al.*, 2004]. Further mineral/mineral partition coefficients ($^{min1/min2}D_{element}$) for Li (Figures 6a and 6c) based on analyses of mineral rims in contact with each other yield values similar to those derived from equilibrated peridotite xenoliths [*Eggins et al.*, 1998; *Seitz and Woodland*, 2000]. Group II sample Ke 1958/20 recrystallized and re-equilibrated at high temperatures [*Kaeser et al.*, 2006] (Table 1). Although cryptically metasomatized (see section 2.2), minerals in this xenolith can be interpreted to be in complete chemical equilibrium as indicated by the lack of zoning with respect to all trace (including Li, Be and B; see Figures 3c and 3d) and major elements including those with very slow diffusivities such as Al [e.g., *Sautter et al.*, 1988] (see profiles of *Kaeser et al.* [2006]). Intermineral D_{Li} values calculated from this sample are in good agreement with equilibrium partition coefficients ($D_{Li\ eq.}$) from the literature [*Brenan et al.*, 1998a; *Seitz and Woodland*, 2000; *Kaliwoda*, 2004; *Ottolini et al.*, 2004]. We therefore used D_B and D_{Be} values based on this sample as estimates of $D_{B\ eq.}$ and $D_{Be\ eq.}$ between ol, cpx and opx (the green lines and *D* values in Figure 6).

[21] Minerals from the other Group II sample (Ke 1958/13) and from the Group I lherzolite are compositionally different with respect to major and trace elements [*Kaeser et al.*, 2006] and are not equilibrated (Figures 3a and 3b). Nevertheless, rim pairs indicate that light elements are similarly distributed as in the equilibrated Group II xenolith (except Be between cpx and opx; Figure 6f). Thus the different *P-T* evolution and metasomatic modification of the three samples had only a subtle effect on the light element systematics.

4.2. Group III

[22] In contrast to Group I and II, ''primary,'' cryptically metasomatized silicates (ol-I, cpx-I, opx-I) in Group III xenoliths are enriched in light elements compared to normal mantle values (Figure 6). Comparison with *D* values derived from the equilibrated Group II xenolith indicates disequilibrium, with respect to both mineral cores and mineral rims (Figure 6).

[23] Also, calculated $^{amph/phl}D$ values (1.00 for Li, 2.95 for Be and 3.84 for B) indicate disequilibrium with respect to light elements when compared to $D_{eq.}$ from experiments (i.e., 0.51, 3.78 and 0.76, respectively, for basanitic systems at 1050°C and 2.0 GPa [*Adam and Green*, 2006]). This is in agreement with disequilibrium indicated by other trace elements (e.g., LREEs, Zr, Hf [see *Kaeser et al.*, 2007]). Disequilibrium partitioning also accounts in most cases for silicate microlites (Ol_m and Cpx_m) in melt pockets, which show large scattering on mineral/mineral plots (Figure 6).

[24] Also, calculated $^{mineral/melt}D_{Be}$ and D_B values based on the composition of microlites (Cpx_m and Ol_m) and silicate glass indicate disequilibrium partitioning as they yield values that cover the entire range of published mineral/melt partition coefficients obtained at different *P-T-X* conditions (see Figure 7 for references). Only D_{Li} derived from Cpx_m/glass pairs yield values in good agreement with experimental data (Figure 7). This may be explained by the combination of the small grain

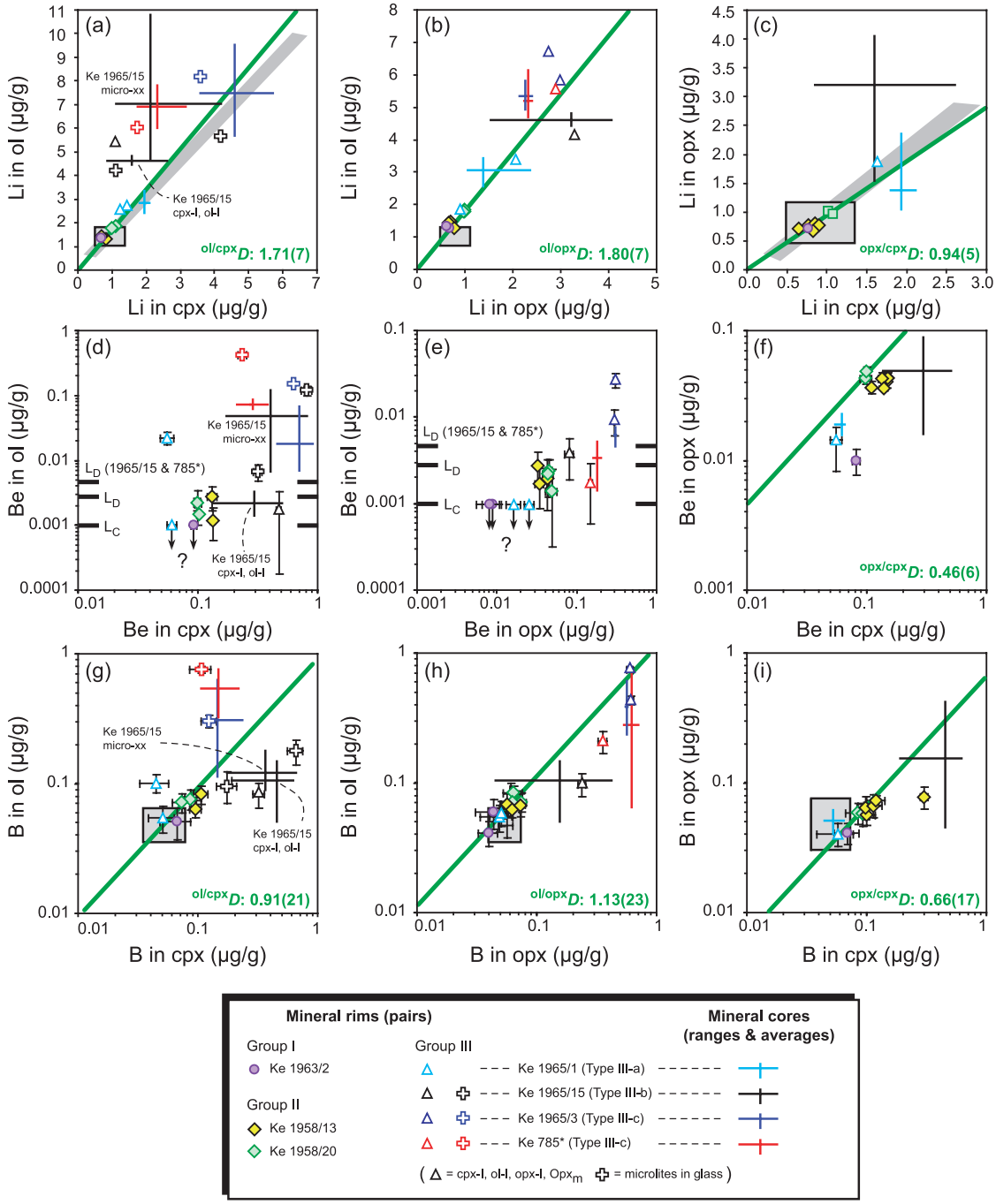

Figure 6. Partitioning of Li, Be, and B between (a, d, and g) olivine and clinopyroxene, (b, e, and h) olivine and orthopyroxene, and (c, f, and i) orthopyrxoxene and clinopyroxene. Symbols correspond to mineral pairs in direct contact with each other. Annotated partition coefficients (*D* values and corresponding thick green lines) are calculated from mineral rim pairs of the completely equilibrated Group II sample Ke 1958/20 (for further details, see text; numbers in brackets are fully propagated errors (last significant digits)). The grey rectangles correspond to the "normal mantle" values of *Seitz and Woodland* [2000] and *Ottolini et al.* [2004]. The light grey fields in Figures 6a and 6c correspond to equilibrium partitioning of *Seitz and Woodland* [2000]. Be concentrations in olivine (Figures 6d and 6e) are mostly between L_D and L_C [see *Currie*, 1968] and therefore are only of qualitative value; note higher L_D for samples Ke 1965/15 and 785* due to shorter analysis times (see Appendix A). Be concentrations below L_C are indicated with an arrow.

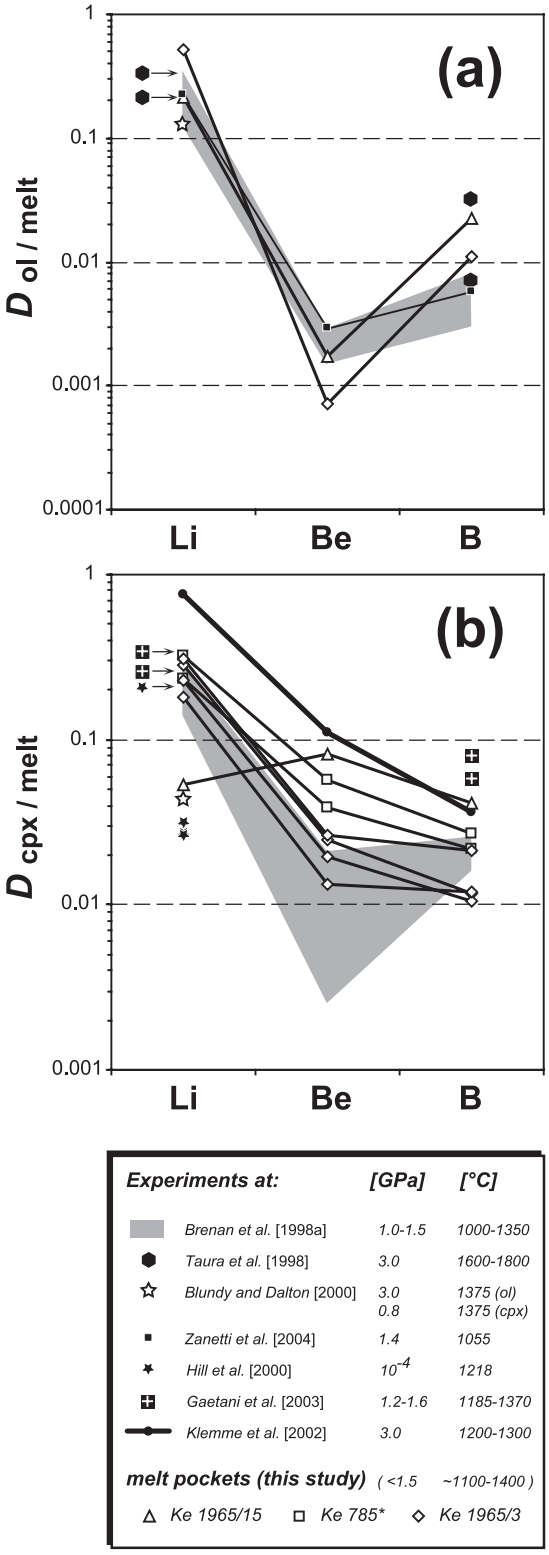

Figure 7. Partitioning of Li, Be, and B between (a) Ol_m and (b) Cpx_m microlites and silicate glass from melt pockets in Type III-b and -c xenoliths from Marsabit compared to experimentally derived equilibrium mineral/melt partition coefficients (note that experiments from *Taura et al.* [1998] at P > 3 GPa are not plotted).

sizes of microlites (<200 μm) and very high diffusivity of Li in melts [e.g., *Richter et al.*, 2003] and minerals [*Coogan et al.*, 2005]. In diopside, for example, Li self diffusion is several orders of magnitude faster than for other cations (e.g., Ca and Mg [see *Coogan et al.*, 2005]). The diffusion of B and Be has only been investigated in Si-rich melts [*Jambon and Semet*, 1978; *Mungall et al.*, 1999] indicating diffusion coefficients ~10 orders of magnitude lower than in the case of Li [*Richter et al.*, 2003]. Strong compositional zoning of microlites with respect to major elements (e.g., Na_2O and Cr_2O_3 in Cpx_m [*Kaeser et al.*, 2007]) is in line with the interpretation that complete equilibration of microlites with the melt was never reached for most elements.

[25] In summary, light element systematics in all minerals from the metasomatized spl harzburgite (Type III-a to -c) point to important disequilibrium processes compared to normal mantle partitioning and exhibit heterogeneity on small scales.

5. Causes for Disequilibrium: Evaluation of Zoning Profiles

5.1. Very Late-Stage Mineral-Melt/Fluid Interaction

[26] Besides Li self-diffusion in clinopyroxene, Mg-Fe inter diffusion in olivine [e.g., *Chakraborty*, 1997] is also very fast compared to diffusion of other elements (e.g., Ca, Al or REEs in clinopyroxene [*Sautter et al.*, 1988; *van Orman et al.*, 2001]). Therefore preservation of zoning patterns for Li (in pyroxenes and olivine) and Mg# (in Type III-c olivines) in mantle rocks indicates that the event responsible for chemical modification was short-lived and occurred during late-stage processes shortly before the rocks quickly cooled to temperatures where further diffusive re-equilibration effectively stops. In the case of mantle xenoliths such rapid cooling only takes place once xenolith-bearing magmas are erupted to the surface. This is in agreement with the presence of quenched melt now preserved as fresh glass.

[27] Using experimentally determined diffusion coefficients (e.g., *Coogan et al.* [2005] for Li in cpx and *Chakraborty* [1997] for Fe-Mg in olivine) and on the basis of the assumption that zoning is solely due to diffusive re-equilibration, the observed profiles can be fitted to simple diffusion models based on the solution of Fick's second law for diffusion in a sphere (see Figure 8 caption for

details). This approach is certainly simplified, as factors such as the crystallographic orientation of mineral grains were not taken into account and effects such as resorbed or overgrown mineral rims are difficult to assess (e.g., there is textural evidence of growth of new Ol_m at the expense of ol-I rims; see Figure 1d). Nevertheless, these models can be used to obtain a rough estimate of the duration of melt- or fluid-rock interaction. The results shown in Figure 8 indicate that rimward Li depletion such as in cpx-I from sample Ke 1965/1 could be produced in several days, even at the low temperatures at which this xenolith partly re-equilibrated (834 ± 37°C; Table 1). Mg-Fe zoning of Type III-c olivine (xenolith Ke 1965/3) in contact with glass would be achieved in the orders of few years (Figure 8). This estimate is even a maximum value as this calculation is based on relatively low temperatures during mineral-melt reaction and comparatively low Mg-Fe interdiffusion coefficients based on experiments conducted at low oxygen fugacities (10^{-12} bars [*Chakraborty*, 1997]). Considering the temperature uncertainty of the mineral-melt reaction event (1246 ± 136°C; based on the olivine-spinel thermometer of *Ballhaus et al.* [1991], using the composition of Chr_m and Ol_m microlites; see Table 1) and higher diffusion coefficients at higher oxygen fugacities [*Gaetani and Watson*, 2000], durations could be even shorter, in the order of several days (not shown), similar to the Li diffusion model for Type III-a cpx. These results are in good agreement with similar models for the formation of silicate glass-bearing melt pockets in mantle xenoliths [e.g., *Shaw and Klügel*, 2002; *Shaw et al.*, 2006].

[28] Yet, diffusion rates of Li in olivine are not constrained experimentally. However, Li (and occasionally B) concentrations in Type III-c olivines are zoned over similar distances as Mg#, suggesting that diffusivities of Li, B and Mg-Fe in olivine are in the same orders of magnitude.

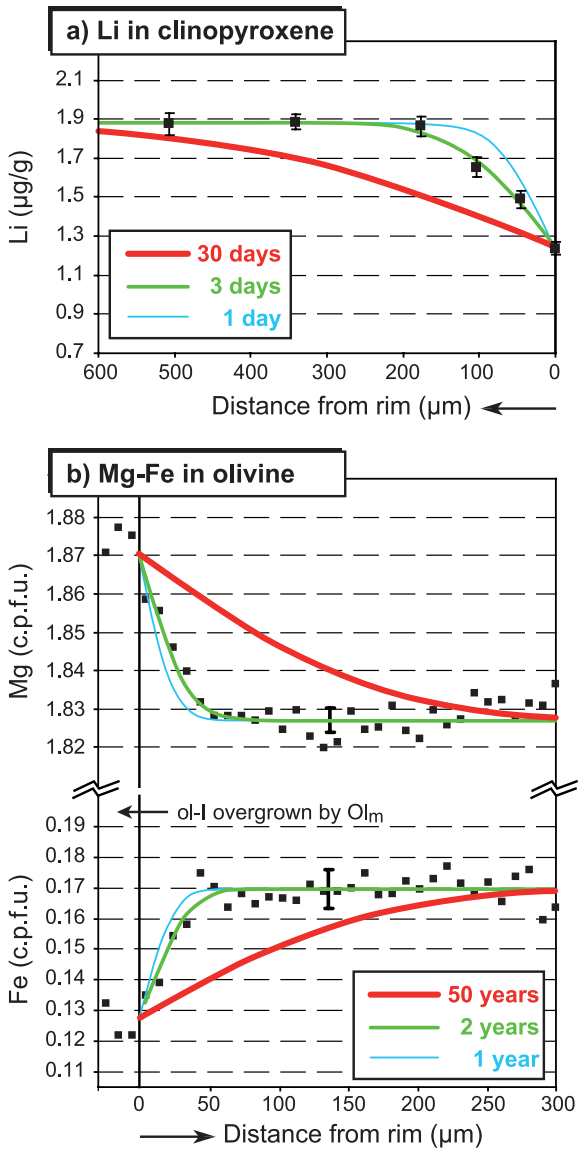

Figure 8. Diffusion models of (a) Li self-diffusion in diopside and (b) Mg-Fe interdiffusion in olivine compared to analyzed Li profiles in cpx-I from Type III-a sample Ke 1965/1 (the right part of the profile depicted in Figure 4a) and Mg-Fe profiles in ol-I from Type III-c sample Ke 1965/3. Models are based on the solution of Fick's second law for diffusion in a sphere. Assuming an open system process maintaining a constant rim composition, this can be written as $[(C_x - C_1)/(C_0 - C_1)] = \mathrm{erfc}[x/2(Dt)^{1/2}]$, where C_x is the element concentration at the distance x from the contact; C_0 is the element concentration at the contact $x = 0$; C_1 is the element concentration in the mineral's core; D is the diffusion coefficient; t is the duration of the diffusion event; and erfc is the complementary error function [*Crank*, 1975]. In the Figure 8a model, Li diffusion ($D = 1.952*10^{-14}$ m^2/s, calculated after *Coogan et al.* [2005]) was modeled at the "final temperature stage" of sample Ke 1965/1 (834°C; see Table 1); in the Figure 8b model, Mg-Fe interdiffusion was modeled using a diffusion coefficient of 5.5×10^{-18} m^2/s (at 1100°C for olivine with Mg# = 92 [*Chakraborty*, 1997]). Error bars in Figure 8a correspond to 2σ of single Li analyses and in Figure 8b to 1σ of the average olivine core composition. For further details, see text.

5.2. Origin of Li Enrichment and Depletion

[29] As outlined above, the well expressed Li zoning profiles in all phases with contacts toward glass (Figures 3a and 5) indicate ongoing very late-stage diffusional re-equilibration with a melt. This type of zoning is similar to grain-scale Li heterogeneity reported from peridotite xenoliths from San Carlos (USA) and far-east Russia [*Jeffcoate et al.*, 2007; *Rudnick and Ionov*, 2007]. In both studies, increasing Li concentrations toward mineral rims (accompanied by Li-isotope fractionation) is interpreted to reflect late-stage peridotite-melt (or fluid) interaction. This interpretation is in agreement with diffusion models and petrographic evidence from this study.

[30] Li depletion of glass-free pyroxene rims, on the other hand, needs another explanation. We did not find clear evidence to which process this is related; however, four different hypotheses can be invoked:

[31] 1. Li zoning is not solely the result of simple diffusion but is related to the major element composition of pyroxenes (i.e., incorporation mechanisms of Li in pyroxene, such as coupled substitutions).

[32] 2. Li zoning is the result of rapid cooling of the xenolith (e.g., after eruption at the Earth's surface).

[33] 3. Li is lost as a result of late-stage in situ partial melting of clinopyroxene during heating and decompression of the xenolith in the host magma.

[34] 4. Li diffuses out of cpx-I (and opx-I) rims as a result of fluid or vapor percolation along grain boundaries and cracks opened by brittle fracturing during rapid xenolith decompression in the host magma.

[35] As shown in the following, hypotheses 1 and 2 are less likely to play an important role. We therefore favor an explanation based on diffusional Li loss either as a result of small degree late clinopyroxene melting or of fluid and/or vapor percolation along grain boundaries.

[36] Hypothesis 1 (substitution mechanisms) would be supported by the fact that some profiles show zoning of major elements (e.g., Na and $Al^{[IV]}$) over the same distances as for Li. Major element zoning in these samples is interpreted to reflect cooling from medium to low mantle temperatures ($\sim$900°C to $\sim$800°C [*Kaeser et al.*, 2006]), which occurred prior to late-stage mineral-melt/fluid reaction [*Kaeser et al.*, 2007]. These low temperatures are, however, still high enough to allow fast Li self-diffusion in cpx [*Coogan et al.*, 2005] (Figure 8). In other words, if Li abundances were initially modified during coupled temperature-dependent major element modification, this effect would be most likely obliterated during later self-diffusive re-equilibration. Summarizing, we believe that the effects of fast Li diffusion are much more important in controlling Li zoning patterns, especially when compared with effects of substitutions of traces of Li coupled with major elements (e.g., cpx with <2 μg/g Li compared to around 10'000 μg/g Na).

[37] Subsolidus Li modification upon late cooling (hypothesis 2) can possibly be excluded as Li loss in pyroxenes should be accommodated by Li gain in another phase, such as olivine (e.g., if $^{ol/cpx}D_{Li}$ is temperature-dependent). This is, however, never observed. Further, also cpx-I – cpx-I contacts (e.g., Figure 3a) show Li depletion, which cannot be explained by simple cooling.

[38] We therefore remain with hypotheses 3 (cpx-I melting) and 4 (fluid or vapor percolation). Clinopyroxene melting has been invoked to explain "spongy" clinopyroxene rims from lavas [*Hibbard and Sjöberg*, 1994] and xenoliths [e.g., *Franz and Wirth*, 1997; *Carpenter et al.*, 2002; *Shaw et al.*, 2006], and would be in line with the occurrence of similar textures observed in this study (Figure 1f). However, this does not explain Li depletion of opx-I rims, which show no sign of melting.

[39] Alternatively, it may be speculated that Li-poor fluid or vapor percolation along grain boundaries and cracks led to continuous leaching of Li from pyroxenes. Given the low D_{Li} for both cpx/fluid and opx/fluid [e.g., *Brenan et al.*, 1998b], this could explain Li depletion in both cpx-I and opx-I. Volatile-rich fluids and vapor exsolution from magma are known to be important factors of triggering xenolith entrapment [e.g., *Lensky et al.*, 2006, and references therein], and brittle fracturing of the xenoliths, allowing vapor and fluid to percolate, is indicated by their friable aspect.

[40] Both late decompression melting (hypothesis 3) and fluid/vapor percolation (hypothesis 4) would have occurred during xenolith transport in the host magma. Ascent of xenolith in basaltic magmas occurs in the order of tens of cm/s [e.g., *Spera*, 1984], implying xenolith-magma interaction of several days to months only (i.e., based of a

maximum sampling depth of <50 km corresponding to <1.5 GPa). These time spans are similar to those calculated from Li diffusion models in diopside (Figure 8). The fact that only pyroxenes but not olivine recorded this process could indicate that Li diffusion coefficients in both cpx and opx are higher than in olivine. This hypothesis is supported by results from other studies which inferred higher diffusivities at least for clinopyroxene compared to olivine [*Jeffcoate et al.*, 2007; *Rudnick and Ionov*, 2007].

6. Comparison Between Light Elements and REEs: Implications for Metasomatic Signatures

[41] Previous trace element investigation (using LA-ICPMS [see *Kaeser et al.*, 2006, 2007]) on all samples included in this study allows us to compare the systematics of light elements with those of ''classical'' trace elements, such as the REEs. In this respect, *Ottolini et al.* [2004] proposed a plot of Li/Yb versus Ce/B in peridotitic clinopyroxene in order to identify different types of metasomatized peridotite and to define the Li-B versus REE systematics of the (hypothetical) ''non-metasomatized'' subcontinental lithospheric mantle (SCLM). Similar plots are illustrated in Figure 9, showing Li/Yb, Ce/B, as well as B/Be ratios of clinopyroxene and amphibole from all samples analyzed in this study. Amphibole is included as Type III-c xenoliths lack primary cpx-I, thus amphibole becomes the major host of REEs in mantle peridotite [e.g., *Eggins et al.*, 1998]. As LA-ICPMS analyses for mineral rims are not always available, only mineral core compositions are taken into account (except for cpx-I in the Group I xenolith which is characterized by strong core-rim zoning of HREEs; see below). Figure 9 shows that amphibole and clinopyroxene cover a large spectrum in terms of Li/Yb, Ce/B and B/Be ratios. Especially in the case of Li/Yb, this includes signatures inferred to be typical for mantle peridotite that has interacted with fluids released from subducting oceanic lithosphere (i.e., characterized by low Ce/B and high Li/Yb and B/Be ratios; see details below). In the following, the significance of these light element/REE signatures for the metasomatic history of the different xenolith groups will be discussed. We will show (1) that strongly varying Li/Yb values can result from both subsolidus mineral reactions and late-stage mineral-melt reaction (melt pocket formation) and (2) that low Ce/B and B/Be possibly simply reflect the signature of any type of metasomatizing fluid, which is not necessarily related to a subducting slab.

6.1. Group I Xenoliths: Effects of Subsolidus Processes

[42] Although the Group I lherzolites contain minor Ti-pargasite and phlogopite, their constituent cpx-I are LREE-depleted and compare well with the signature found in typical nonmetasomatized peridotite [*Eggins et al.*, 1998; *Kaeser et al.*, 2006]. In line with this, light element concentrations in cpx-I (as well as in ol-I and opx-I) fall within the range of the ''normal mantle'' values (Figure 6) [*Seitz and Woodland*, 2000]). Consequently, as expected, their Ce/B ratio is in good agreement with the SCLM estimate of *Ottolini et al.* [2004]. On the other hand, the low HREE contents in the cores of cpx-I from Group I lherzolites result in Li/Yb ratios higher than SCLM (Figure 9a). This is, however, obviously due to the preservation of a garnet-facies signature preserved in the Group I clinopyroxenes, as reflected by core-rim zoning of HREEs (i.e., Yb in cpx-I of sample Ke 1963/2 Yb increases from ~0.17 to ~4.15 μg/g [*Kaeser et al.*, 2006]). Consequently, Li/Yb variation in this case does not imply metasomatism but reflects subsolidus HREE repartitioning during the garnet-spinel transition (see *Ionov* [2004] for similar subsolidus REE fractionation processes). This highlights that Li/Yb ratios of clinopyroxene can only be applied to discriminate melt signatures from different tectonic settings when other processes such as subsolidus decoupling of Li from Yb can be clearly excluded.

6.2. Group II Xenoliths: Effects of High-*T* Metasomatism

[43] Clinopyroxenes from the two heated and recrystallized Group II lherzolites (Ke 1958/13 and 1958/20) are LREE-enriched [*Kaeser et al.*, 2006]. In contrast, the light element abundances are only slightly higher than in LREE-depleted Group I lherzolites (Figure 2), resulting only in small deviations from the SCLM (Figure 9a) or ''normal mantle'' fields (Figure 6). Restricted intergrain and intragrain variability, with respect to both REEs [*Kaeser et al.*, 2006] and light elements (Figure 2) as well as mineral/mineral *D* values close to inferred equilibrium partition coefficients (Figure 6 and section 4.1), indicates that during this high-temperature metasomatizing event, minerals nearly equilibrated with the percolating melt. On the basis of REE patterns of calculated melts in equilibrium with Group II

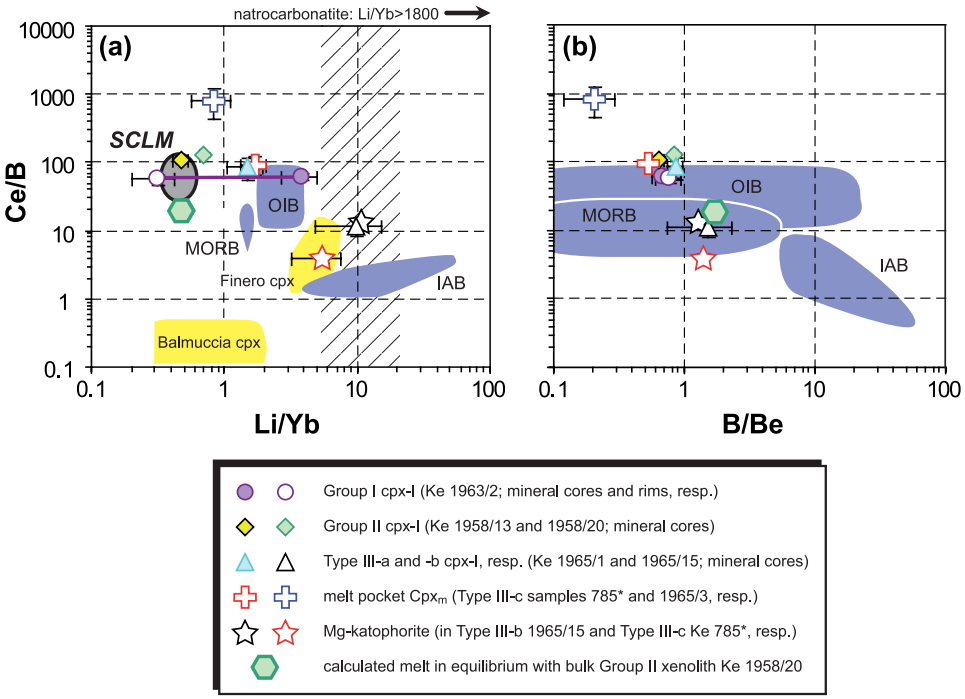

Figure 9. (a) Li/Yb versus Ce/B and (b) B/Be versus Ce/B ratios in clinopyroxene, Mg-katophorite, and calculated melt in equilibrium with the bulk modal composition of the equilibrated Group II xenolith Ke 1958/20 (using Li, Be, and B mineral/melt partition coefficients of *Brenan et al.* [1998a]). For the calculation of the Ce and Yb concentrations, see *Kaeser et al.* [2006, and references therein]. Literature data in Figure 9a: SCLM (subcontinental lithospheric mantle), MORB, and OIB as in the work of *Ottolini et al.* [2004]. Hachured field corresponds to Li/Yb ratios of melilitite and nephelinite from Oldoinyo Lengai [*Keller et al.*, 2006; *Klaudius and Keller*, 2006]. Natrocarbonatite data from *Halama et al.* [2007]. Finero and Balmuccia clinopyroxene from *Raffone et al.* [2006] and *Ottolini et al.* [2004]. B/Be ratios for MORB and OIB based on data from *Ryan and Langmuir* [1988], *Dostal et al.* [1996], and *Bach et al.* [2001] for Be and on *Ryan and Langmuir* [1993], *Chaussidon and Marty* [1995], *Dostal et al.* [1996], *Tanaka and Nakamura* [2005], and *Gméling et al.* [2007] for B (considering only analyses from MORB with >7 wt% MgO). Field for IAB (Figures 9a and 9b) based on data from the Panama [*Defant et al.*, 1991; *Tomascak et al.*, 2000] and Vanuatu arcs [*Peate et al.*, 1997].

xenoliths, we proposed earlier that Group II lherzolites interacted with a basanitic or alkali-basaltic melt of an already evolved composition, resulting from chromatographic trace element fractionation [*Kaeser et al.*, 2006]. Such a calculated melt in equilibrium with the completely homogenized Group II xenolith Ke 1958/20 would have 4.9 μg/g Li, 3.2 μg/g Be and 5.8 μg/g B (using the average Li, Be and B of ol-I, opx-I, and cpx-I, bulk partition coefficients based on mineral/melt D values of *Brenan et al.* [1998a] and relative modal abundances as given in Table 1; spinel was neglected due to low modal abundances). These values compare well with typical light element budgets of OIB type intraplate basaltic rocks [e.g., *Ryan and Langmuir*, 1987; *Dostal et al.*, 1996; *Ryan et al.*, 1996; *Ryan and Kyle*, 2004; *Tanaka and Nakamura*, 2005; *Gméling et al.*, 2007]. This also holds true for Ce/B and B/Be of the hypothetical melt (Figure 9b), but not for the Li/Yb ratio, which is significantly lower (~0.5) than in any typical mantle-derived melt (Figure 9a). This apparent mismatch can be explained by chromatographic trace element fractionation processes during which elements with strongly different bulk rock/melt partition coefficients will be fractionated from each other [e.g., *Navon and Stolper*, 1987]. Using the modal composition of xenolith Ke 1958/20, the bulk partition coefficient ratio for Li and Yb (D_{Li}/D_{Yb}) is ~3 while D_{Ce}/D_B is ~1 and D_B/D_{Be} is ~0.6. This implies that during chromatographic trace element fractionation, Li will be effectively fractionated from Yb, while fractionation of B, Be and Ce is more limited. Consequently, more evolved liquids will still reflect the Ce/B and B/Be ratios of the initial (or primary) metasomatizing melt. The slightly elevated Ce/B ratios of the Group II clinopyroxene (compared to the SCLM; Figure 9a) are in line with this interpretation and coincide with other samples interpreted in the context of chromatographic fractionation processes [*Ottolini et al.*,

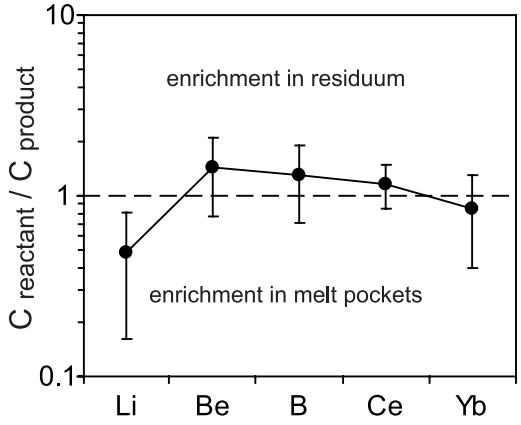

Figure 10. Comparison of the Li, Be, B, Ce, and Yb budget in the bulk melt pockets of Type III-c xenolith Ke 785* ($C_{product}$: glass + Cpx_m + Ol_m) and in residual phases ($C_{reactant}$: amphibole ± phlogopite ± Opx_m) preserved in melt pockets. Trace element budgets were calculated using the average trace element compositions of phases (error bars correspond to fully propagated errors) and relative phase proportions obtained from major element–based mass balance calculations performed in order to explain melt pocket formation by incongruent partial melting of precursor phases (0.820 amphibole + 0.102 phlogopite + 0.078 Opx_m = 0.350 glass + 0.329 Ol_m + 0.322 Cpx_m; least squares fitting; sum of squared residuals = 0.35; see *Kaeser et al.* [2007] for details). The results show that melt pocket formation by fluid-induced melting occurred under near closed conditions with respect to B, Be, and REEs, whereas Li was added (see text for further details).

2004]. Such a subtle effect on Ce/B and B/Be can be expected as long as no agent with strongly differing B and Be solubilities (e.g., hydrous fluids), and no minerals able to fractionate these trace elements are present. Amphibole crystallization, for example, would potentially lead to increase B/Be ratios in a remaining fluid or melt (due to $^{amph/melt}D_B < D_{Be}$ [*Brenan et al.*, 1998a]).

6.3. Group III Xenoliths: Light Element Redistribution During Melt Pocket Formation

[44] Minerals from Group III harzburgite and dunite show the strongest light element enrichment (Figures 2 and 6) and cpx-I (where present) and amphibole are characterized by fractionated light element/REE ratios (Figure 9). However, these minerals are all associated with late-stage melt pockets (samples Ke 785* and Ke 1965/15; see Table 1). Therefore the effect of late melt pocket formation on the light element and REE budget of preexisting cpx-I and amphibole has to be assessed, before their initial light element signature can be discussed.

[45] Textures indicate that melt pockets result from incongruent melting of earlier phases induced or triggered by a CO_2-bearing fluid according to a reaction such as

$$\text{(R1)}\quad \text{amph} \pm \text{phl} \pm \text{opx} + CO_2 = Cpx_m + Ol_m + Chr_m + \text{Mg-calcite} + \text{melt}$$

Similar processes related to melt pocket formation in mantle xenoliths were described by *Ionov et al.* [1994] and *Ban et al.* [2005], for example. Mass balance calculations based on major elements show that during this process, the bulk melt pockets inherited large parts of the major and trace element budget of the precursor phases (mainly amphibole; see Figure 10 caption and *Kaeser et al.* [2007] for details). The only component added in greater quantities is CO_2 (now stored in Mg-calcite). However, rimward modification of primary minerals adjacent to melt pockets supposes that exchange with the melt occurred at least to some extent and that melt pockets are not closed systems with respect to all components. We tested this hypothesis on the example of xenolith Ke 785*, by applying the mass balance parameters derived from major elements to the light elements, as well as to Ce and Yb. The result is illustrated in Figure 10, which shows that reaction (1) preserved (within errors) the trace element budget with respect to B, Be, Ce and Yb, whereas Li concentrations are higher in bulk melt pockets than in the precursor phases involved in reaction (1). This indicates metasomatic Li addition during melt pocket formation, probably by the CO_2-bearing fluid inferred from major element mass balance. Mantle-derived CO_2-rich liquids can be extremely Li-enriched, as shown in studies of Li systematics in natrocarbonatite melt from Oldoinyo Lengai, for example (211–292 μg/g Li and Li/Yb >1880 [*Simonetti et al.*, 1997; *Halama et al.*, 2007]; see Figure 9a). Such melts or fluids (note that natrocarbonatite is interpreted by some authors to represent condensed CO_2-rich fluid [*Nielsen and Veksler*, 2002]) may therefore be effective agents for Li metasomatism in the mantle.

[46] Decoupling of Li from other trace elements is in agreement with light element zoning in Mg-katophorite (Figure 5c), characterized by increasing Li contents toward rims, while B and Be profiles are flat. Such zoning indicate that the relic

precursor phases in melt pockets no longer preserve their original Li/Yb ratios. Consequently high Li/Yb values in Group III xenoliths cannot be used to determine the metasomatizing agent responsible for earlier amphibole formation. In contrast, the mobility of B, Be and REEs during late-stage melting is restricted compared to Li. In the case of B, this is illustrated by its very heterogeneous distribution in melt pocket phases of different textural context on a very small scale (e.g., comparatively B-poor Ol_m microlites or selvages on ol-I form at the expense of B-poor Opx_m; see Figures 1d and 5a). This makes Ce/B and B/Be ratios more robust tracers for the amphibole-forming metasomatizing event than Li/Yb.

6.4. Is There a Subduction-Related Component in the Group III Harzburgites?

[47] Concluding from the above descriptions, Li enrichment during melt pocket formation obliterated the geochemical signature of earlier metasomatic phases with respect to Li/Yb ratios, whereas Ce, Be and B were less affected. However, Li concentration in the cores of large ol-I porphyroclasts from Group III samples, away from enriched rims, are still significantly higher than expected for unmetasomatized peridotite [*Seitz and Woodland*, 2000; *Ottolini et al.*, 2004] (see Figure 6). This, together with elevated B/Be and low Ce/B ratios of cpx-I and amphibole presumably unaffected by late metasomatism, raises the question whether the metasomatizing agent was a fluid or melt released from subducting lithosphere. On the basis of the enrichment of Li and B in subducting slabs compared to the depleted upper mantle [*Ryan and Langmuir*, 1987; *Leeman and Sisson*, 2002], slab-released fluids would preferentially enrich the overlying mantle wedge in Li and B compared to REEs and Be [e.g., *Paquin et al.*, 2004; *Scambelluri et al.*, 2006; *Raffone et al.*, 2006]. Such fluids would further explain other geochemical features of amphibole and cpx-I in Type III-b and -c xenoliths such as high REE/HFSE ratios [*Kaeser et al.*, 2007], resulting from low HFSE solubilities in hydrous fluids and/or presence of HFSE-rich minerals (e.g., rutile) in the residual subducting slab [e.g., *Brenan et al.*, 1995; *Keppler*, 1996; *Stalder et al.*, 1998; *Klemme et al.*, 2005; *Kessel et al.*, 2005]. Similar metasomatic signatures in mantle samples from tectonic settings above or close to subduction zones are commonly interpreted to result from the percolation of slab-derived melts or fluids [e.g., *Maury et al.*, 1992; *Kepezhinskas et al.*, 1996; *Grégoire et al.*, 2001; *Laurora et al.*, 2001; *Parkinson et al.*, 2003].

[48] On the other hand, the last tectonic event that potentially led to subduction-related metasomatism in the lithospheric mantle beneath Marsabit was the formation of the East African Orogen in Pan-African times (720–550 Myr [e.g., *Meert*, 2003]). In contrast to this, early metasomatism in the Group III samples is texturally young, and clearly overprints the penetratively deformed fabric of the premetasomatic "protolith" [*Kaeser et al.*, 2006]. Deformation and associated decompression and cooling were attributed to Mesozoic rifting (formation of the Anza Graben [*Kaeser et al.*, 2006]). Metasomatism must thus be related to the Tertiary-Quaternary magmatic activity at Marsabit. Consequently, if the early metasomatic assemblage in Group III xenoliths contains a subduction-related component, it must be an old mantle domain modified by ancient slab fluids that remelted in the Tertiary-Quaternary. Preliminary Pb and Sr isotope data on minerals from sample Ke 785*, however, do not point to any "slab-related" component (E. Bourdon, personal communication, 2006). Whatever the origin of the light element enrichment in Marsabit is, we would like to emphasize that it is in any case not straightforward to postulate "subduction signatures" based only on trace element patterns from single minerals, especially in cases where ample evidence for extensive melt-rock reaction and disequilibrium processes exists (such as the Group III xenoliths; see Figures 6 and 9). Especially "slab-tracers" such as Li isotopes and Li/Yb ratios in mantle minerals from tectonic settings away from any present-day subduction zone are particularly prone to be modified by later metasomatism related to intraplate magmatism that ultimately led to xenolith entrapment. This can be the result of diffusive Li isotope fractionation [*Jeffcoate et al.*, 2007; *Rudnick and Ionov*, 2007] and diffusive decoupling of Li from Yb during late-stage mineral-melt reaction as shown in this study (see section 6.3). Alternatively, there is growing evidence that other effective metasomatizing agents such as CO_2-rich and Si-undersaturated melts like melilitites and nephelinites [*Keller et al.*, 2006; *Klaudius and Keller*, 2006], carbonatites [*Cooper et al.*, 1995] and natrocarbonatites [*Simonetti et al.*, 1997; *Halama et al.*, 2007] can have very high Li/Yb ratios as well.

[49] Also, low Ce/B and elevated B/Be ratios in metasomatic phases prior to late melting (see

Figures 9 and 10) do not necessarily imply the impact of slab fluids. There are several recent studies which highlight the potential of melt-rock reaction, reactive porous flow and chromatographic trace element fractionation to produce such residual volatile-enriched Si-rich and even carbonated fluids of variously enriched trace element composition starting from relatively "ordinary" mantle melts including intraplate alkali basalts or basanites [e.g., *Bedini et al.*, 1997; *Xu et al.*, 1998; *Ionov et al.*, 2002; *Bodinier et al.*, 2004; *Rivalenti et al.*, 2004]. A similar fluid could have led to the crystallization of volatile-bearing phases assemblage in Group III-b and -c xenoliths (Mg-katophorite, phlogopite, apatite, graphite), while the presence of Opx_m at low mantle pressures (<1.5 GPa) excludes other metasomatizing agents such as carbonatitic melts [e.g., *Lee and Wyllie*, 2000]. Given the expected highly fluid-mobile character of B compared to REEs or Be [e.g., *Brenan et al.*, 1998b; *Kessel et al.*, 2005], metasomatic minerals forming from such evolved fluids would be expected to have low Ce/B and high B/Be and thus "slab-like" signatures.

7. Summary and Conclusions

[50] 1. The Li-Be-B systematics in minerals from unmetasomatized, deformed, decompressed and cooled Group I lherzolite are similar to other estimates on the light element content of unmetasomatized peridotite. Highly variable Li/Yb values of clinopyroxene are not a metasomatic signature but can be explained by subsolidus garnet breakdown (HREE repartitioning).

[51] 2. Light element abundances in minerals from reheated and cryptically metasomatized Group II lherzolite deviate only slightly from values typical for unmetasomtized lherzolite. Calculated melts in equilibrium with an equilibrated Group II xenolith have relatively low light element abundances, similar to those of typical intraplate alkali basaltic magmas. This is in agreement with calculated REE patterns of melts in equilibrium with Group II xenoliths, which are similar to Tertiary-Quaternary alkali basalts and basanites that ultimately transported the xenoliths to the surface [*Kaeser et al.*, 2006].

[52] 3. In contrast, modal metasomatism in Group III harzburgite and dunite shows evidence for addition of light elements by evolved volatile- and Si-rich fluids and/or melts during EARS-related metasomatism in the shallow lithospheric mantle. Light element signatures such as Li/Yb, Ce/B and B/Be ratios are similar to what would be expected for minerals in mantle peridotite metasomatized by fluids/melts containing a slab-derived component. However, mass balance calculations and simple diffusion models show that late melting/crystallization events (i.e., the formation of typical melt pockets) can strongly modify the light element systematics in mantle xenoliths. This is especially the case for the very fast diffusing element Li. Interpreting Li systematics (including Li isotopes [see *Jeffcoate et al.*, 2007; *Rudnick and Ionov*, 2007]) thus necessitates careful knowledge of late-stage features, especially in the case of mantle xenolith as they often react with their host magma [e.g., *Shaw et al.*, 2006]. If late metasomatic events last longer than several days or occur at higher temperatures, Li diffusion may quickly obliterate older signatures and becomes decoupled from other trace elements. Interpretation of trace element ratios, such as the widely used Li/Yb values, is therefore prone to error.

[53] 4. High B/Be and low Ce/B ratios in Group III amphibole and clinopyroxene most likely reflect metasomatism by a fluid phase with low Be and REE solubilities compared to B. This, together with evidences for diffusive Li decoupling from REEs indicates that geochemical fingerprints similar to "slab signatures" (with respect to the light elements in minerals) are possibly not distinctive.

Appendix A: Analytical Methods

[54] Li, Be and B concentrations in silicates (olivine, orthopyroxene, clinopyroxene, amphibole, phlogopite) and silicate glass were measured in situ, on polished thin sections by Secondary Ion Mass Spectrometry (SIMS) using a modified CAMECA IMS 3f ion microprobe (Mineralogisches Institut, Universität Heidelberg, Germany), equipped with a primary beam mass filter. A 14.5 keV/20 nA $^{16}O^-$ primary ion beam was used. The surface imaged by the secondary ions was reduced from $\sim$30 μm to $\sim$12 μm by applying a field aperture (FA2; 750 μm). Positive secondary ions were accelerated to a nominal energy of 4.5 keV and the mass spectrometer's energy window was set to 40 eV. Secondary ^{7}Li, ^{9}Be, and ^{11}B ions were collected applying the energy filtering method [*Ottolini et al.*, 1993] using an offset of 75 eV at a mass resolution ($m/\Delta m$) of $\sim$1030. The applied offset allows minimization of the matrix effects [see *Ottolini et al.*, 1993, Figure 2], while the chosen mass resolutions allow differentiation between ^{7}Li ions and ^{6}LiH molecules. The intensities were

normalized to the count rates of ^{30}Si and calibrated against the NIST SRM610 glass standard (concentrations from *Pearce et al.* [1997]). SiO_2 (wt%) concentrations in the respective phase were obtained by electron microprobe analysis. Secondary ion intensities were measured using an electron multiplier in counting mode, which is linear to count rates of at least $2*10^5$ s^{-1}. The lower limit of linearity is set by the spectrometer's and the counting system's background. Concentrations in both samples and standards lie well within the linear range of the counting system. Using the SRM610 as standard (and not the SRM612 with ~1/10 concentration) allows for a better precision of the calibration. The relative reproducibility was <1% [*Marschall et al.*, 2006]. The accuracy is limited by matrix effects and the uncertainty of the element concentrations in the reference material. The accuracy is estimated to be <20% [*Ottolini et al.*, 1993]. One analysis comprises 10 cycles for each element with an integration time of 8 s/cycle for Li, 16 s/cycle for Be and B, and 2 s/cycle for Si. The total analysis time was ~12 min (including ~400 s presputtering). Typical background counting times are $\sim 2*10^{-2}$ cps (corresponding to ~1 ng/g Li and Be and ~3 ng/g B). The minimal detectable values (i.e., the detection limit L_D of *Currie* [1968]) are 4.7 ng/g Li, 2.9 ng/g Be, and 7.5 ng/g B (two samples, Ke 1965/15 and Ke 785*, have been analyzed with 4 s/cycle for Li and 8 s/cycle for Be and B, which increases the minimal detectable values to 7.7 ng/g Li, 4.7 ng/g Be, and 12.1 ng/g B). Count numbers of a cpx analysis in sample Ke 1963/2, for example, are in the order of 30 cps (^7Li), 3 cps (^9Be), 0.5 cps (^{11}B) and ~50'000 cps (^{30}Si).

[55] As SIMS is a method were material is removed from a polished surface, contamination, especially in the case of boron [*Shaw et al.*, 1988], is always present. Owing to this and to the generally low concentrations of Li, Be and B in mantle rocks, careful sample preparation is essential. Thin sections for this study have been prepared at the Institute of Mineralogy (University of Heidelberg, Germany) following a standard protocol to minimize surface contamination [*Marschall and Ludwig*, 2004]. Pure glycol was used as lubricant and cooling liquid for sawing and polishing and all products containing boric acid were avoided. Samples were then coated with carbon for BSE investigation (textures) and electron microprobe analyses (major element composition of minerals; see above). After this, the carbon was removed using γ-alumina powder and distilled water. Subsequently, the samples were cleaned in an ultrasonic bath using ultra-pure water from a Milli-Q water purification system (Millipore). Ultrasonic cleaning was repeated three times for about 10 min. Thin sections were then coated with gold. During SIMS analysis, presputtering further removes possible surface contamination. Applying the field aperture that limits the imaged field's diameter to less than the diameter of the primary beam avoids that surface contamination at the sputtering crater's edge reaches the mass spectrometer. Following this procedure described by *Marschall and Ludwig* [2004], the boron contamination level is <2 ng/g. Lithium contamination is typically ~50 times lower than for boron, and beryllium does not show any sign of contamination.

Acknowledgments

[56] This work was financially supported by the Swiss National Science Foundation (grant 200021-100647/1 to A.K.). Field work in Kenya was financially supported by the Deutsche Forschungsgemeinschaft within the frame of the Collaborative Research Centre 108 (RFB 108) at the University of Karlsruhe. Fruitful discussions with Erwan Bourdon, Rainer Altherr, Dmitri Ionov, Alan Woodland, and Othmar Müntener helped to improve an earlier version of this paper. Ilona Fin and Oliver Wienand (Heidelberg) are thanked for the preparation of top-quality thin sections for SIMS analysis. We gratefully acknowledge constructive reviews by Tim Elliott, Ralf Halama, and an anonymous reviewer as well as helpful comments from the editors Vincent Salters and Glenn Gaetani.

References

Adam, J., and T. Green (2006), Trace element partitioning between mica- and amphibole-bearing garnet lherzolite and hydrous basanitic melt: 1. Experimental results and the investigation of controls on partitioning behaviour, *Contrib. Mineral. Petrol.*, *152*, 1–17.

Bach, W., J. C. Alt, Y. L. Niu, S. E. Humphris, J. Erzinger, and H. J. B. Dick (2001), The geochemical consequences of late-stage low-grade alteration of lower ocean crust at the SW Indian Ridge: Results from ODP Hole 735B (Leg 176), *Geochim. Cosmochim. Acta*, *65*, 3267–3287.

Ballhaus, C., R. F. Berry, and D. H. Green (1991), High pressure experimental calibration of the olivine-orthopyroxene-spinel oxygen geobarometer: Implications for the oxidation state of the upper mantle, *Contrib. Mineral. Petrol.*, *107*, 27–40.

Ban, M., G. Witt-Eickschen, M. Klein, and H. A. Seck (2005), The origin of glasses in hydrous mantle xenoliths from the West Eifel, Germany: Incongruent break down of amphibole, *Contrib. Mineral. Petrol.*, *148*, 511–523.

Bebout, G. E., J. G. Ryan, and W. P. Leeman (1993), B-Be Systematics in subduction-related metamorphic rocks: Characterization of the subducted component, *Geochim. Cosmochim. Acta*, *57*, 2227–2237.

Bedini, R. M., J.-L. Bodinier, J.-M. Dautria, and L. Morten (1997), Evolution of LILE-enriched small melt fractions in the lithospheric mantle: A case study from the East African Rift, *Earth Planet. Sci. Lett.*, *153*, 67–83.

Blundy, J., and J. Dalton (2000), Experimental comparison of trace element partitioning between clinopyroxene and melt in carbonate and silicate systems, and implications for mantle metasomatism, *Contrib. Mineral. Petrol.*, *139*, 356–371.

Bodinier, J.-L., M. A. Menzies, N. Shimizu, F. A. Frey, and E. McPherson (2004), Silicate, hydrous and carbonate metasomatism at Lherz, France: Contemporaneous derivates of silicate melt-harzburgite reaction, *J. Petrol.*, *45*, 299–320.

Brenan, J. M., H. F. Shaw, F. J. Ryerson, and D. L. Phinney (1995), Mineral-aqueous fluid partitioning of trace elements at 900°C and 2.0 GPa: Constraints on the trace element chemistry of mantle and deep crustal fluids, *Geochim. Cosmochim. Acta*, *59*, 3331–3350.

Brenan, J. M., E. Neroda, C. C. Lundstrom, H. F. Shaw, F. J. Ryerson, and D. L. Phinney (1998a), Behaviour of boron, beryllium, and lithium during melting and crystallization: Constraints from mineral-melt partitioning experiments, *Geochim. Cosmochim. Acta*, *62*, 2129–2141.

Brenan, J. M., F. J. Ryerson, and H. F. Shaw (1998b), The role of aqueous fluids in the slab-to-mantle transfer of boron, beryllium, and lithium during subduction: Experiments and models, *Geochim. Cosmochim. Acta*, *62*, 3337–3347.

Brey, G. P., and T. Köhler (1990), Geothermobarometry in four-phase lherzolites II. New thermobarometers, and practical assessment of existing thermobarometers, *J. Petrol.*, *31*, 1353–1378.

Brooker, R. A., R. H. James, and J. D. Blundy (2004), Trace element and Li isotope systematics in Zabargad peridotites: Evidence of ancient subduction processes in the Red Sea mantel, *Chem. Geol.*, *212*, 179–204.

Carpenter, R. L., A. D. Edgar, and Y. Thibault (2002), Origin of spongy textures in clinopyroxene and spinel from mantle xenoliths, Hessian Depression, Germany, *Mineral. Petrol.*, *74*, 149–162.

Carroll Webb, S. A., and B. J. Wood (1986), Spinel-pyroxene-garnet relationship and their dependence on Cr/Al ratio, *Contrib. Mineral. Petrol.*, *92*, 471–480.

Chakraborty, S. (1997), Rates and mechanisms of Fe-Mg interdiffusion in olivine at 980–1300°C, *J. Geophys. Res.*, *102*, 12,317–12,331.

Chan, L. H., and M. Kastner (2000), Lithium isotopic compositions of pore fluids and sediments in the Costa Rica subduction zone: Implications for fluid processes and sediment contribution to the arc volcanoes, *Earth Planet. Sci. Lett.*, *183*, 275–290.

Chaussidon, M., and B. Marty (1995), Primitive boron isotope composition of the mantle, *Science*, *269*, 383–386.

Coogan, L. A., S. A. Kasemann, and S. Chakraborty (2005), Rates of hydrothermal cooling of new oceanic upper crust derived from lithium-geospeedometry, *Earth Planet. Sci. Lett.*, *240*, 415–424.

Cooper, A. F., L. A. Paterson, and D. L. Reid (1995), Lithium in carbonatites: Consequence of an enriched mantle source, *Mineral. Mag.*, *59*, 401–408.

Crank, J. (1975), *The Mathematics of Diffusion*, 2nd ed., Clarendon, Oxford, U. K.

Currie, L. A. (1968), Limits for qualitative detection and quantitative determination, *Anal. Chem.*, *40*, 586–593.

Defant, M. J., P. M. Richerson, J. Z. Deboer, R. H. Stewart, R. C. Maury, H. Bellon, M. S. Drummond, M. D. Feigenson, and T. E. Jackson (1991), Dacite genesis via both slab melting and differentiation: Petrogenesis of La Yeguada volcanic complex, Panama, *J. Petrol.*, *32*, 1101–1142.

Dostal, J., C. Dupuy, and P. Dudoignon (1996), Distribution of boron, lithium and beryllium in ocean island basalts from French Polynesia: Implications for the B/Be and Li/Be ratios as tracers of subducted components, *Mineral. Mag.*, *60*, 563–580.

Eggins, S. M., R. L. Rudnick, and W. F. McDonough (1998), The composition of peridotites and their minerals: A laser-ablation ICP-MS study, *Earth Planet. Sci. Lett.*, *154*, 53–71.

Elliott, T. (2003), Tracers of the slab, in *Inside the Subduction Factory*, *Geophys. Monogr. Ser.*, vol. 138, edited by J. Eiler, pp. 23–45, AGU, Washington, D. C.

Elliott, T., A. Jeffcoate, and C. Bouman (2004), The terrestrial Li isotope cycle: Light-weight constraints on mantle convection, *Earth Planet. Sci. Lett.*, *220*, 231–245.

Elliott, T., A. Thomas, A. Jeffcoate, and Y. L. Niu (2006), Lithium isotope evidence for subduction-enriched mantle in the source of mid-ocean-ridge basalts, *Nature*, *443*, 565–568.

Franz, L., and R. Wirth (1997), Thin intergranular melt films and melt pockets in spinel peridotite xenoliths from the Rhön area (Germany): Early stage of melt generation by grain boundary melting, *Contrib. Mineral. Petrol.*, *129*, 268–283.

Gaetani, G. A., and E. B. Watson (2000), Open system behaviour of olivine-hosted melt inclusions, *Earth Planet. Sci. Lett.*, *183*, 27–41.

Gaetani, G. A., A. J. R. Kent, T. L. Grove, I. D. Hutcheon, and E. M. Stolper (2003), Mineral/melt partitioning of trace elements during hydrous peridotite partial melting, *Contrib. Mineral. Petrol.*, *145*, 391–405.

Gméling, K., K. Nemeth, U. Martin, N. Eby, and Z. Varga (2007), Boron concentrations of volcanic fields in different geotectonic settings, *J. Volcanol. Geotherm. Res.*, *159*, 70–84.

Grégoire, M., B. I. A. McInnes, and S. Y. O'Reilly (2001), Hydrous metasomatism of oceanic sub-arc mantle, Lihir, Papua New Guinea, Part 2. Trace element characteristics of slab-derived fluids, *Lithos*, *59*, 91–108.

Halama, R., W. F. McDonough, R. L. Rudnick, J. Keller, and J. Klaudius (2007), The Li isotopic composition of Oldoinyo Lengai: Nature of the mantle sources and lack of isotopic fractionation during carbonatite petrogenesis, *Earth Planet. Sci. Lett.*, *254*, 77–89.

Henjes-Kunst, F., and R. Altherr (1992), Metamorphic petrology of xenoliths from Kenya and northern Tanzania and implications for geotherms and lithospheric structures, *J. Petrol.*, *33*, 1125–1156.

Hibbard, M. J., and J. J. Sjöberg (1994), Signs of incongruent melting of clinopyroxene in limburgite, Thetford Hill, Vermont, *Can. Mineral.*, *32*, 307–317.

Hill, E., B. J. Wood, and J. D. Blundy (2000), The effect of Ca-Tschermaks component on trace element partitioning between clinopyroxene and silicate melt, *Lithos*, *53*, 203–215.

Ionov, D. A. (2004), Chemical variations in peridotite xenoliths from Vitim, Siberia: Inferences for REE and Hf behaviour in the garnet-facies upper mantle, *J. Petrol.*, *45*, 343–367.

Ionov, D. A., A. W. Hofmann, and N. Shimizu (1994), Metasomatism-induced melting in mantle xenoliths from Mongolia, *J. Petrol.*, *35*, 753–785.

Ionov, D. A., J.-L. Bodinier, S. B. Mukasa, and A. Zanetti (2002), Mechanisms and sources of mantle metasomatism: Major and trace element compositions of peridotite xenoliths

from Spitsbergen in the context of numerical modelling, *J. Petrol.*, *43*, 2219–2259.

Ishikawa, T., and E. Nakamura (1994), Origin of the slab component in arc lavas from across-arc variation of B and Pb isotopes, *Nature*, *370*, 205–208.

Jambon, A., and M. P. Semet (1978), Lithium diffusion in silicate-glasses of albite, orthoclase, and obsidian composition—Ion-microprobe determination, *Earth Planet. Sci. Lett.*, *37*, 445–450.

Jeffcoate, A. B., T. Elliott, S. A. Kasemann, D. Ionov, K. Cooper, and R. Brooker (2007), Li isotope fractionation in peridotites and mafic melts, *Geochim. Cosmochim. Acta*, *71*, 202–218.

Kaeser, B., A. Kalt, and T. Pettke (2006), Evolution of the lithopsheric mantle beneath the Marsabit volcanic field (northern Kenya): Constraints from textural, P-T and geochemical studies on xenoliths, *J. Petrol.*, *47*, 2149–2184.

Kaeser, B., A. Kalt, and T. Pettke (2007), Crystallisation and breakdown of metasomatic phases in graphite-bearing peridotite xenoliths from Marsabit (Kenya), *J. Petrol.*, doi:10.1093/petrology/egm036.

Kaliwoda, M. (2004), Mantel-Xenolithe des Harrat Uwayrid (Saudi-Arabien): Archive des stofflichen und thermischen Entwicklung des lithopshärischen Erdmantels im Bereich eines passiven Kontinentalrandes, Ph.D. thesis, 365 pp., Univ. of Heidelberg, Heidelberg, Germany.

Keller, J., A. N. Zaitsev, and D. Wiedenmann (2006), Primary magmas at Oldoinyo Lengai: The role of olivine melilitites, *Lithos*, *91*, 150–172.

Kepezhinskas, P., M. J. Defant, and M. S. Drummond (1996), Progressive enrichment of island arc mantle by melt-peridotite interaction inferred from Kamchatka xenoliths, *Geochim. Cosmochim. Acta*, *60*, 1217–1229.

Keppler, H. (1996), Constraints from partitioning experiments on the composition of subduction-zone fluids, *Nature*, *380*, 237–240.

Kessel, R., M. W. Schmidt, P. Ulmer, and T. Pettke (2005), Trace element signature of subduction-zone fluids, melts and supercritical liquids at 120–180 km depth, *Nature*, *437*, 724–727.

Klaudius, J., and J. Keller (2006), Peralkaline silicate lavas at Oldoinyo Lengai, Tanzania, *Lithos*, *91*, 173–190.

Klemme, S., J. D. Blundy, and B. J. Wood (2002), Experimental constraints on major and trace element partitioning during partial melting of eclogite, *Geochim. Cosmochim. Acta*, *66*, 3109–3123.

Klemme, S., S. Prowatke, K. Hametner, and D. Gunther (2005), Partitioning of trace elements between rutile and silicate melts: Implications for subduction zones, *Geochim. Cosmochim. Acta*, *69*, 2361–2371.

Laurora, A., M. Mazzucchelli, G. Rivalenti, R. Vannucci, A. Zanetti, M. A. Barbieri, and C. A. Cingolani (2001), Metasomatism and melting in carbonated peridotite xenoliths from the mantle wedge: The Gobernador Gregores case (southern Patagonia), *J. Petrol.*, *42*, 69–87.

Lee, W. J., and P. J. Wyllie (2000), The system CaO-MgO-SiO_2-CO_2 at 1 Gpa, metasomatic wehrlites, and primary carbonatite magmas, *Contrib. Mineral. Petrol.*, *138*, 214–228.

Leeman, W. P., and V. B. Sisson (2002), Geochemistry of boron and its implications for crustal and mantle processes, in *Boron: Mineralogy, Petrology and Geochemistry*, *Rev. Mineral. Geochem.*, vol. 33, edited by E. S. Grew and L. M. Anovitz, pp. 645–708, Mineral. Soc. of Am., Washington, D. C.

Lensky, N. G., R. W. Niebo, J. R. Holloway, V. Lyakhovsky, and O. Navon (2006), Bubble nucleation as a trigger for xenolith entrapment in mantle melts, *Earth Planet. Sci. Lett.*, *245*, 278–288.

Lundstrom, C. C., M. Chaussidon, A. T. Hsui, P. Kelemen, and M. Zimmerman (2005), Observations of Li isotopic variations in the Trinity Ophiolite: Evidence for isotopic fractionation by diffusion during mantle melting, *Geochim. Cosmochim. Acta*, *69*, 735–751.

Marschall, H. R., and T. Ludwig (2004), The low-boron contest: Minimising surface contamination and analysing boron concentrations at the ng/g-level by secondary ion mass spectrometry, *Mineral. Petrol.*, *81*, 265–278.

Marschall, H., R. Altherr, T. Ludwig, A. Kalt, K. Gméling, and Z. Kasztovszky (2006), Partitioning and budget of Li, Be and B in high-pressure metamorphic rocks, *Geochim. Cosmochim. Acta*, *70*, 4750–4769.

Maury, R. C., M. J. Defant, and J. L. Joron (1992), Metasomatism of the sub-arc mantle inferred from trace-elements in Philippine xenoliths, *Nature*, *360*, 661–663.

Meert, J. G. (2003), A synopsis of events related to the assembly of eastern Gondwana, *Tectonophysics*, *362*, 1–40.

Morley, C. K., R. A. Day, R. Lauck, R. Bosher, D. M. Stone, S. T. Wigger, W. A. Wescott, D. Haun, N. Bassett, and W. Bosworth (2006), Geology and geophysics of the Anza Graben, in *Geoscience of Rift Systems—Evolution of East Africa*, edited by C. K. Morley, *AAPG Stud. Geol.*, *44*, 67–90.

Mungall, J. E., D. B. Dingwell, and M. Chaussidon (1999), Chemical diffusivities of 18 trace elements in granitoid melts, *Geochim. Cosmochim. Acta*, *63*, 2599–2610.

Navon, O., and E. Stolper (1987), Geochemical consequences of melt percolation: The upper mantle as a chromatographic column, *J. Geol.*, *95*, 285–307.

Nielsen, T. F. D., and I. V. Veksler (2002), Is natrocarbonatite a cognate fluid condensate?, *Contrib. Mineral. Petrol.*, *142*, 425–435.

Nishio, Y., S. Nakai, J. Yamamoto, H. Sumino, T. Matsumoto, V. S. Prikhod'ko, and S. Arai (2004), Lithium isotopic systematics of the mantle-derived ultramafic xenoliths: Implications for EM1 origin, *Earth Planet. Sci. Lett.*, *217*, 245–261.

Ottolini, L., P. Bottazzi, and R. Vannucci (1993), Quantification of lithium, beryllium, and boron in silicates by secondary ion mass spectrometry using conventional energy filtering, *Anal. Chem.*, *65*, 1960–1968.

Ottolini, L., B. Le Fèvre, and R. Vannucci (2004), Direct assessment of mantle boron and lithium contents and distribution by SIMS analyses of peridotite minerals, *Earth Planet. Sci. Lett.*, *228*, 19–36.

Paquin, J., R. Altherr, and T. Ludwig (2004), Li-Be-B systematics in the ultrahigh-pressure garnet peridotite from Alpe Arami (central Swiss Alps): Implications for slab-to-mantle wedge transfer, *Earth Planet. Sci. Lett.*, *218*, 507–519.

Parkinson, I. J., R. J. Arculus, and S. M. Eggins (2003), Peridotite xenoliths from Grenada, Lesser Antilles island arc, *Contrib. Mineral. Petrol.*, *146*, 241–262.

Parkinson, I. J., S. J. Hammond, R. H. James, and N. W. Rogers (2007), High-temperature lithium isotope fractionation: Insights from lithium isotope diffusion in magmatic systems*Earth Planet. Sci. Lett.*, *257*, 609–621, doi:10.1016/j.epsl.2007.03.023.

Peacock, S. M., and R. L. Hervig (1999), Boron isotopic composition of subduction-zone metamorphic rocks, *Chem. Geol.*, *160*, 281–290.

Pearce, N. J. G., W. T. Perkins, J. A. Westgate, M. P. Gorton, S. E. Jackson, C. R. Neal, and S. P. Chenery (1997), A com-

pilation of new and published major and trace element data for NIST SRM 610 and NIST SRM 612 glass reference materials, *Geostand. Newsl.*, *21*, 115–144.

Peate, D. W., J. A. Pearce, C. J. Hawkesworth, H. Colley, C. M. H. Edwards, and K. Hirose (1997), Geochemical variations in Vanuatu arc lavas: The role of subducted material and a variable mantle wedge composition, *J. Petrol.*, *38*, 1331–1358.

Raffone, N., B. Le Fèvre, L. Ottolini, R. Vannucci, and A. Zanetti (2006), Light-lithophile element metasomatism of Finero peridotite (W Alps): A secondary-ion mass spectrometry study, *Microchim. Acta*, *155*, 251–255.

Richter, F. M., A. M. Davis, D. J. DePaolo, and E. B. Watson (2003), Isotope fractionation by chemical diffusion between molten basalt and rhyolite, *Geochim. Cosmochim. Acta*, *67*, 3905–3923.

Rivalenti, G., A. Zanetti, M. Mazzucchelli, R. Vannucci, and C. A. Cingolani (2004), Equivocal carbonatite markers in the mantle xenoliths of the Patagonia backarc: The Gobernador Gregores case (Santa Cruz Province, Argentina), *Contrib. Mineral. Petrol.*, *147*, 647–670.

Rudnick, R. L., and D. A. Ionov (2007), Lithium elemental and isotopic disequilibrium in minerals from peridotite xenoliths from far-east Russia: Product of melt/fluid-rock reaction, *Earth Planet. Sci. Lett.*, *256*, 278–293.

Ryan, J. G., and P. R. Kyle (2004), Lithium abundance and lithium isotope variations in mantle sources: Insights from intraplate volcanic rocks from Ross Island and Marie Byrd Land (Antarctica) and other oceanic islands, *Chem. Geol.*, *212*, 125–142.

Ryan, J. G., and C. H. Langmuir (1987), The systematics of Lithium abundances in young volcanic rocks, *Geochim. Cosmochim. Acta*, *51*, 1727–1741.

Ryan, J. G., and C. H. Langmuir (1988), Beryllium systematics in young volcanic rocks: Implications for ^{10}Be, *Geochim. Cosmochim. Acta*, *52*, 237–244.

Ryan, J. G., and C. H. Langmuir (1993), The systematics of boron abundances in young volcanic rocks, *Geochim. Cosmochim. Acta*, *57*, 1489–1498.

Ryan, J. G., W. P. Leeman, J. D. Morris, and C. H. Langmuir (1996), The boron systematics of intraplate lavas: Implications for crust and mantle evolution, *Geochim. Cosmochim. Acta*, *60*, 415–422.

Sautter, V., O. Jaoul, and F. Abel (1988), Aluminum diffusion in diopside using the ^{27}Al (p, γ)^{28}Si nuclear reaction: Preliminary results, *Earth Planet. Sci. Lett.*, *23*, 109–114.

Scambelluri, M., J. Fiebig, N. Malaspina, O. Müntener, and T. Pettke (2004), Serpentinite subduction: Implications for fluid processes and trace-element recycling, *Int. Geol. Rev.*, *46*, 595–613.

Scambelluri, M., J. Hermann, L. Morten, and E. Rampone (2006), Melt- versus fluid-induced metasomatism in spinel to garnet wedge peridotites (Ulten Zone, Eastern Italian Alps): Clues from trace element and Li abundances, *Contrib. Mineral. Petrol.*, *151*, 372–394.

Seitz, H.-M., and A. B. Woodland (2000), The distribution of lithium in peridotitic and pyroxenitic mantle lithologies—An indicator of magmatic and metasomatic processes, *Chem. Geol.*, *166*, 47–64.

Seitz, H.-M., G. P. Brey, Y. Lahaye, S. Durali, and S. Weyer (2004), Lithium isotopic signatures of peridotite xenoliths and isotopic fractionation at high temperature between olivine and pyroxenes, *Chem. Geol.*, *212*, 163–177.

Shaw, C. S., and A. Klügel (2002), The pressure and temperature conditions and timing of glass formation in mantle-derived xenoliths from Baarley, West Eifel, Germany: The case for amphibole breakdown, lava infiltration and mineral-melt reaction, *Mineral. Petrol.*, *74*, 163–187.

Shaw, D. M., M. D. Higgins, M. G. Truscott, and T. A. Middleton (1988), Boron contamination in polished thin-sections of meteorites: Implications for other trace-element studies by alpha-track image or ion microprobe, *Am. Mineral.*, *73*, 894–900.

Shaw, C. S. J., F. Heidelbach, and D. B. Dingwell (2006), The origin of reaction textures in mantle peridotite xenoliths from Sal Island, Cape Verde: The case for "metasomatism" by the host lava, *Contrib. Mineral. Petrol.*, *151*, 681–697.

Simonetti, A., K. Bell, and C. Shrady (1997), Trace- and rare-earth-element geochemistry of the June 1993 natrocarbonatite lavas, Oldoinyo Lengai (Tanzania): Implications for the origin of carbonatite magmas, *J. Volcanol. Geotherm. Res.*, *75*, 89–106.

Spera, F. J. (1984), Carbon-dioxide in petrogenesis. 3. Role of volatiles in the ascent of alkaline magma with special reference to xenolith-bearing mafic lavas, *Contrib. Mineral. Petrol.*, *88*, 217–232.

Stalder, R., S. F. Foley, G. P. Brey, and I. Horn (1998), Mineral aqueous fluid partitioning of trace elements at 900–1200°C and 3.0–5.7 GPa: New experimental data for garnet, clinopyroxene, and rutile, and implications for mantle metasomatism, *Geochim. Cosmochim. Acta*, *62*, 1781–1801.

Tanaka, R., and E. Nakamura (2005), Boron isotopic constraints on the source of Hawaiian shield lavas, *Geochim. Cosmochim. Acta*, *69*, 3385–3399.

Taura, H., H. Yurimoto, K. Kurita, and S. Sueno (1998), Pressure dependence on partition coefficients for trace elements between olivine and the coexisting melts, *Phys. Chem. Miner.*, *25*, 469–484.

Tomascak, P. B., J. G. Ryan, and M. J. Defant (2000), Lithium isotope evidence for light element decoupling in the Panama subarc mantle, *Geology*, *28*, 507–510.

Tomascak, P. B., E. Widom, L. D. Benton, S. L. Goldstein, and J. G. Ryan (2002), The control of lithium budgets in island arcs, *Earth Planet. Sci. Lett.*, *196*, 227–238.

van Orman, J. A., T. L. Grove, and N. Shimizu (2001), Rare earth element diffusion in diopside: Influence of temperature, pressure, and ionic radius, and an elastic model for diffusion in silicates, *Contrib. Mineral. Petrol.*, *141*, 687–703.

Woodland, A. B., H.-M. Seitz, and G. M. Yaxley (2004), Varying behaviour of Li in metasomatised spinel peridotite xenoliths from western Victoria, Australia, *Lithos*, *75*, 55–66.

Wunder, B., A. Meixner, R. L. Romer, and W. Heinrich (2006), Temperature-dependent isotopic fractionation of lithium between clinopyroxene and high-pressure hydrous fluids, *Contrib. Mineral. Petrol.*, *151*, 112–120.

Xu, Y. G., M. A. Menzies, J. L. Bodinier, R. M. Bedini, P. Vroon, and J. C. C. Mercier (1998), Melt percolation and reaction atop a plume: Evidence from the poikiloblastic peridotite xenoliths from Boree (Massif Central, France), *Contrib. Mineral. Petrol.*, *132*, 65–84.

Zack, T., P. B. Tomascak, R. L. Rudnick, C. Dalpe, and W. F. McDonough (2003), Extremely light Li in orogenic eclogites: The role of isotope fractionation during dehydration in subducted oceanic crust, *Earth Planet. Sci. Lett.*, *208*, 279–290.

Zanetti, A., M. Tiepolo, R. Oberti, and R. Vannucci (2004), Trace-element partitioning in olivine: Modelling of a complete data set from a synthetic hydrous basanite melt, *Lithos*, *75*, 39–54.